Toward Transition State Analysis of DAHP Synthase

Alvin Niu, B. Pharm.

Department of Biochemistry and Biomedical Sciences, McMaster University

In partial fulfillment of the requirements for the degree Master of Science

McMaster University

Abstract

Antibiotic resistance is a major threat to the global health. The overuse and misuse of antibiotics have accelerated the process of antibiotic resistance and the emergence of multiple drug resistant bacteria. Therefore, it is urgent to develop new antibiotics. 3 Deoxy-D-*arabino*heptulosonate-7-phosphate (DAHP) synthase is a promising target due to its vital role in shikimate pathway in bacteria, and the lack of mammalian counterpart. It catalyzes the aldol-like reaction between erythrose 4-phosphate and phosphoenolpyruvate, the first step in shikimate pathway. Inhibiting DAHPS will disrupt the shikimate pathway, leading to bacteria death. However, no clinical available DAHPS inhibitor makes it important to fully understand DAHPS catalytic mechanism. A tetrahedral intermediate (THI) is formed and broken during the reaction. Two possible mechanisms regarding THI breakdown generate the opposite charge distribution on the transition state (TS). The TS is an ideal target for inhibitor design. Due to the low concentration and short lifetimes, kinetic isotope effects (KIEs) are the only means to determine TS structures in detail. Competitive KIEs measurement involves measurement of the ratio of isotopologues in the same reaction. In this study, we have developed a method for accurate measurement of isotope ratios by quantitative NMR that involves using a less time-consuming pulse program that only flips the magnetization to an 'Ernst angle', and processing the NMR peaks with Voigt deconvolution fitting model which considers both the natural line shapes and the contributions from the spectrometer.

Acknowledgements

I would like to take this opportunity to thank my supervisor, Dr. Paul Berti, for giving the opportunity to work in his lab and providing invaluable guidance throughout the project. He has taught me the scientific methodology to carry out the research and the skills to present the research works. I would also like to thank my committee members, Dr. Russell Bishop and Dr. Anthony Rullo, for the continuous advice.

Also, I would like to thank Dr. Bob Berno, and Dr. Hilary Jenkins in the NMR Facility who kindly provided me with guidance and support on NMR measurements.

Additionally, I would like to thank all Berti lab members both past and present, Dr. Simanga Gama, Dr. Maren Heimhalt, Pallavi Mukherjee, Mandeep Marway, Rebecca Turner, Klara Stringa, Lovette Chan, Victoria Brown, Jessica Mo, Vanessa DiCecco, James Anupol, Claire Willmer, Shahbano Syed, Chris McChesney, and Sabih Jamil. It was an honour to have worked with these intelligent, industrious and inspiring people.

Finally, my sincere gratitude to my family for their unconditional love and support. This would not have been possible without their encouragement and trust in me.

Table of Contents

List of Figures

List of Tables

List of Abbreviations

αCKSs	α-Carboxyketose synthases
A5P	D-arabinose-5-phosphate
ADP	adenosine diphosphate
ATP	adenosine triphosphate
CMP	cytosine monophosphate
CTP	cytidine triphosphate
DAHP	3-deoxy-D-*arabino*-heptulosonate-7-phosphate
DAHPS	DAHP synthase
DFO	deferoxamine B
DIEA	*N, N*-diisopropylethylamine
DTT	*DL*-dithiothreitol
E. coli	*Escherichia coli*
E4P	erythrose 4-phosphate
EDTA	ethylenediaminetetraacetic acid
efp	exponential multiplication/Fourier transform/phase correction
em	exponential multiplication
EPSP	5-enoylpyruvyl shikimate phosphate synthase
FID	free induction decay
FT	Fourier transform
G6P	glucose-6-phosphate
gb	gaussian factor
HPLC	high performance liquid chromatography
HSQC	heteronuclear single quantum coherence
IPTG	isopropyl β-D-1-thiogalactopyranoside
k_{cat}	turnover number
K_i	equilibrium dissociation constant for inhibitor binding
K_M	Michaelis constant
KDO	3-deoxy-D-*manno*-2-octulosonic acid
KDO8P	3-deoxy-D-*manno*-2-octulosonate-8-phosphate
KDO8PS	KDO8P synthase
KIE	kinetic isotope effect
lb	line broadening
LB	lysogeny broth
LDH	lactate dehydrogenase
LFER	linear free energy relationship
LPS	lipopolysaccharides
ManNAc	*N*-acetylmannosamine
MDR	multiple drug resistant

MG/AM	malachite green/ammonium molybdate
MMI	mass and moments of inertia
NAD^+	oxidized nicotinamide adenine dinucleotide
NADH	reduced nicotinamide adenine dinucleotide
NeuB	bacterial sialic acid synthase
NeuNAc	*N*-acetylneuraminic acid
NMR	nuclear magnetic resonance
O1P	transmitter frequency offset for channel F1 in ppm
PEP	phosphoenolpyruvate
Phe	phenylalanine
P_i	inorganic phosphate
PK	pyruvate kinase
ppsA	phosphoenolpyruvate synthetase
qNMR	quantitative nuclear magnetic resonance
rf	radiofrequency
S/N	signal-to-noise ratio
SDS/PAGE	sodium dodecyl sulfate/polyacrylamide gel electrophoresis
SI	size of the real spectrum
SW	spectral Width
TCEP	tris(2-carboxyethyl)phosphine
THI	tetrahedral intermediate
TIM	triose phosphate isomerase
T_R	residence time
Tris	tris(hydroxymethyl)amino methane
Trp	tryptophan
TS	transition state
Tyr	tyrosine
ZPE	zero-point energy

1 Introduction

1.1 Antibiotic resistance

Antibiotics have transformed modern medicine and saved millions of lives since the discovery of penicillin in 1928[1,2]. It was first prescribed in 1940s and heavily used during the second world war[3]. However, resistance appeared in laboratories before it entered clinical use[4]. The penicillin discovery team was able to identify a bacterial penicillinase[5,6], which provides resistance by specifically hydrolysing the β-lactam ring functionality in penicillin. By the 1950s, penicillin resistance had become a clinical problem and threatened the advances of the prior decades[7].

Similar to penicillin, resistance to other antibiotics emerged in the decades after they were introduced to the clinic[7]. Unfortunately, resistance has been seen in almost all antibiotics that have been developed[2]. Antibiotic resistance will eventually emerge even when antibiotics are used correctly, but the misuse and overuse of antibiotics has greatly accelerated the process, and the lack of new antibiotic development makes the problem much worse[8–10]. Antibiotic misuse is widespread; in nearly 50% of cases either the choice of medication or duration of antibiotic therapy is incorrect[11]. Subinhibitory and subtherapeutic antibiotic concentrations lead to antibiotic resistance through genetic alternations, which increases virulence and promotes antibiotic resistance and spread[10]. The three fundamental mechanisms of antibiotics resistance are *(i)* degradation or modification of the antibiotic molecule, *(ii)* decreased membrane permeability or the overexpression of efflux pumps, and *(iii)* protection or alteration of antibiotic target sites[12].

The development of new antibiotics had always been an effective strategy to alleviate the problem of resistance. However, the rate of antibiotic development has decreased since the 1960s due to economic and regulatory obstacles[7,13]. Pharmaceutical companies have cut their investment in developing new antibiotic molecules because they are not very profitable. Antibiotics are inherently used for short periods, and newly approved antibiotics are often reserved for use as a last resort in order to delay the development of resistance. Therefore, only a limited number of new antibiotics that have been discovered over the last several decades. Most newly introduced antibiotics are just derivatives of previous antibiotics[14]. But they are only useful for a short period, since the emergence of resistance is nearly inevitable. Thus, the development of new antibiotics and new targets is crucially needed.

1.2 α-Carboxyketose synthase family

α-Carboxyketose synthases (αCKSs) have significant roles in bacterial survival and virulence[15]. Members of the family include 3-deoxy-D-*arabino*heptulosonate 7-phosphate (DAHP) synthase (DAHPS), 3-deoxy-D-*manno*octulosonate 8-phosphate synthase (KDO8PS) and NeuB, an *N*-acetylneuraminate synthase[16]. αCKSs catalyze aldol-like condensation reactions using phosphoenolpyruvate (PEP) and an aldose as substrates to form 3-deoxy-2-keto sugars with differing chain lengths (Figure 1.1). DAHPS utilizes erythrose-4-phophaste (E4P) as its aldose substrate, while KDO8PS uses arabinose 5-phosphate (A5P) and NeuB uses *N*-acetylmannosamine.

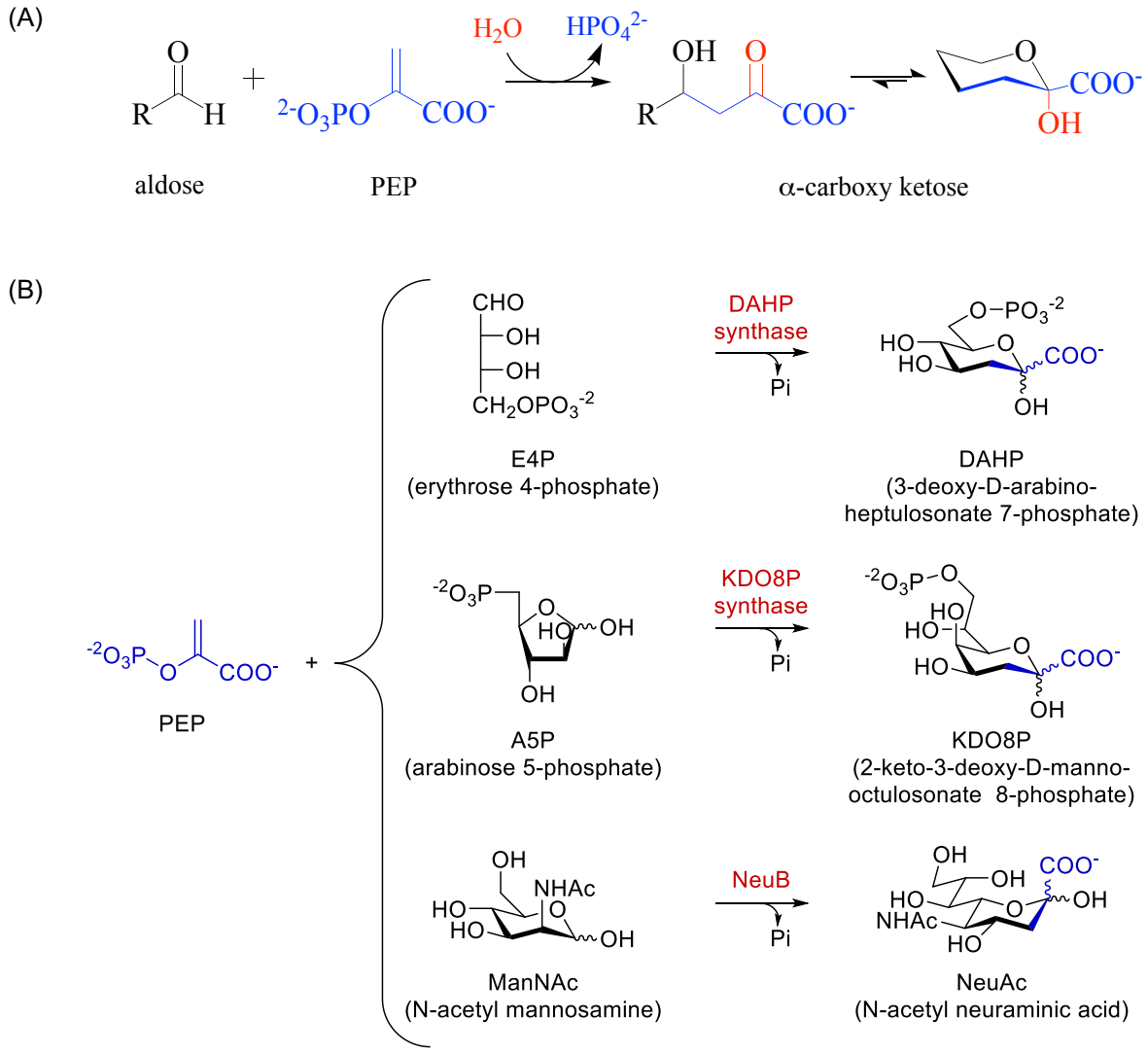

Figure 1.1 αCKSs condensation reactions.

(**A**) General αCKS catalyzes the reaction of an aldose and PEP substrate to form 3-deoxy-2-keto sugars. (**B**) The three main αCKS reactions catalyzed by DAHPS, KDO8P, and NeuB, respectively.

In all these three reactions, inorganic phosphate (P_i) is released from substrate PEP through the breakage of C-O bond. All three members are involved in metabolic processes in bacteria, and are essential for pathogenicity. They are considered to be promising targets for design and development of new antibiotics since they do not exist in mammals.

1.2.1 DAHPS

DAHPS catalyses the reaction between PEP and E4P, to form DAHP and P_i. It is the first enzyme in shikimate pathway, which is present in microorganisms, plants and some fungi, but is absent in higher eukaryotes[17]. It is well regulated by feedback inhibition to control the concentration of downstream reaction products of the pathway[18–20].

1.2.1.1 Shikimate pathway

The shikimate pathway is a seven-step pathway for the biosynthesis of aromatic amino acids in all bacteria and plants. It does not exist in mammals, which makes it a promising target for the development of antibiotics, herbicides and pesticides[21,22]. The pathway starts with DAHPS and finishes with the intermediate chorismate (Figure 1.2). Chorismate is a branch point precursor in the synthesis of tryptophan (Trp) through anthranilate, while in the synthesis of tyrosine (Tyr) and phenylalanine (Phe), prephenate acts as an intermediate[23,24].

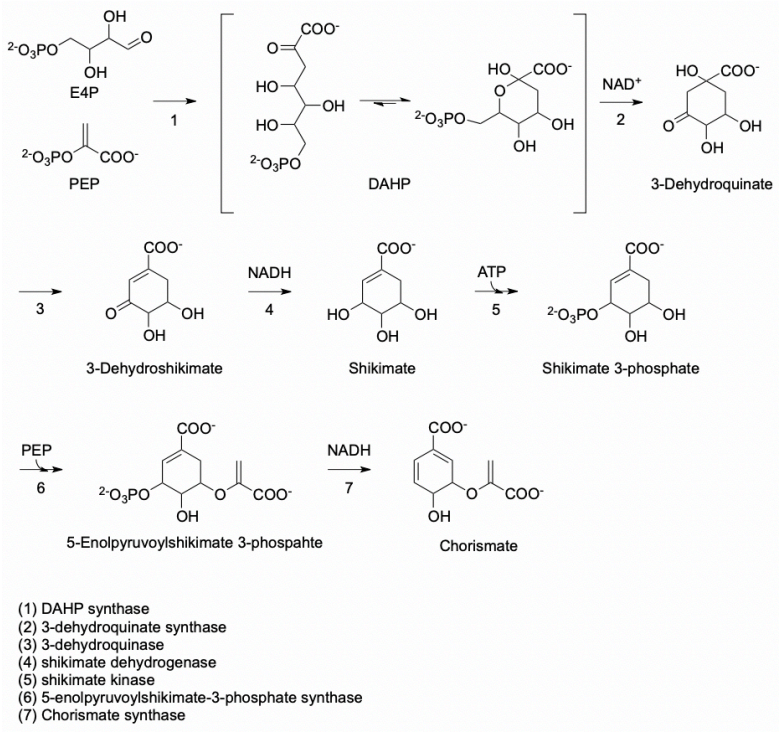

Figure 1.2 Shikimate pathway.

DAHPS catalyzes the first step of shikimate pathway to form DAHP, which is converted to chorismite through six-step reaction. Figure from reference [25].

In addition to aromatic amino acids, the shikimate pathway is also involved in the biosynthesis of several secondary metabolites, including folates, flavonoids, ubiquinone and lignans, which are essential for bacteria survival[26] (Figure 1.3). Therefore, inhibiting the shikimate pathway disrupts the biosynthesis of protein and secondary metabolites, resulting antimicrobial effects. As the first enzyme in the pathway, DAHPS controls the downstream carbon flow through the pathway. As a result, the inhibition of DAHPS would cause the disruption of shikimate pathway, leading to rapid death of bacteria[27].

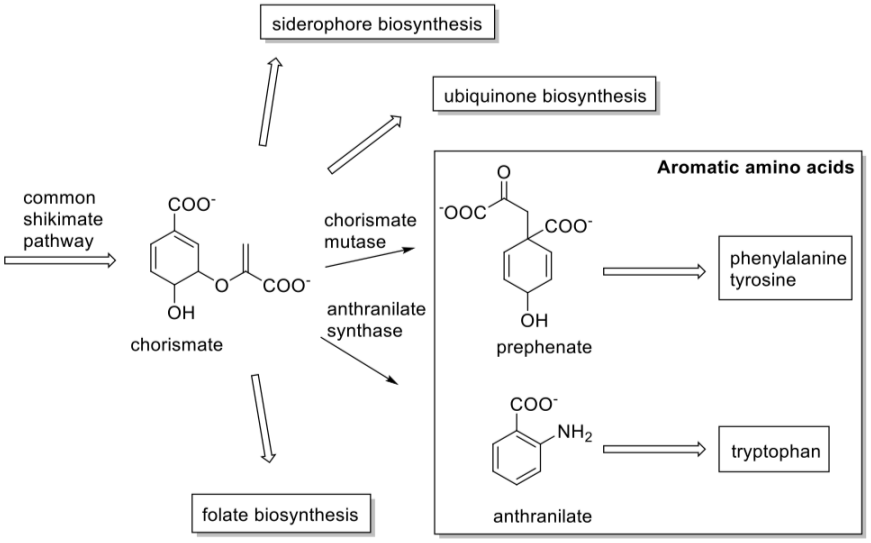

Figure 1.3 Chorismate as a branch point in the synthesis of amino acids and secondary metabolites.

Adapted from Light et al[28].

Shikimate pathway being a target for antibiotics design has been validated in knockout experiments. For example, knocking out the AroA gene, which encodes 5-enolpyruvoylshikimic acid-3-phosphate (EPSP) synthase, the sixth enzyme of the shikimate pathway, rendered *Bordetella bronchiseptica* and *Pseudomonas aeruginosa* nonvirulent[29,30].

In spite of the pathway's importance and potential value as an antimicrobial target, only one commercially useful inhibitor of this pathway has been found, namely the herbicide glyphosate, which targets EPSP synthase[31,32], but it is not an antibiotic. Currently there is no antibiotic targeting shikimate pathway that is used clinically. Thus, our efforts focus on investigating DAHPS as a target of inhibition.

1.2.2 NeuB

NeuB is also a member of αCKS superfamily. It catalyzes the condensation of PEP and *N*-acetylmannosamine, forming *N*-acetylneuraminic acid, a sialic acid. Sialic acids are a family of nine carbon 3-deoxy-2-keto sugars, which are involved in a variety of biological functions[33]. They are widely distributed in mammalian cells, and to a lesser degree, in fungi and bacteria[34]. In mammalian cells, they are found at the end of secreted and cell surface glycoproteins and glycolipids. Due to their location, they play a significant role in cellular recognition and adhesion[35–37]. In addition, they are also correlated with tumorigenesis and metastasis in certain cancers[38,39]. In several pathogenic bacteria, sialic acid is synthesized and located on cell surface to mimic mammalian cells to escape the host's immune system[40]. This includes *Neisseria meningitidis* that causes meningitis[41] and *Campylobacter jejuni* that causes food-borne gastroenteritis[42].

In mammals, ManNAc is first phosphorylated into ManNAc-6-phosphate by ManNAc kinase, followed by NeuNAc-9-phosphate synthase-catalyzed condensation with PEP to form NeuNAc-9-phosphate. NeuNAc-9-phosphate is then dephosphorylated to NeuNAc by NeuNAc-9-phophate phosphatase. In contrast, in bacteria the condensation reaction between ManNAc and PEP catalyzed by NeuNAc synthase, NeuB, generates NeuNAc directly (Figure 1.4)[43]. NeuNAc is then activated using cytosine triphosphate, CTP, to give CMP-NeuNAc, an activated substrate for sialyltransferases that transfer this keto acid to glycoproteins and glycolipids[35]. This difference in the NeuNAc biosynthesis pathway in mammals and bacteria makes NeuB a promising target for inhibitor design.

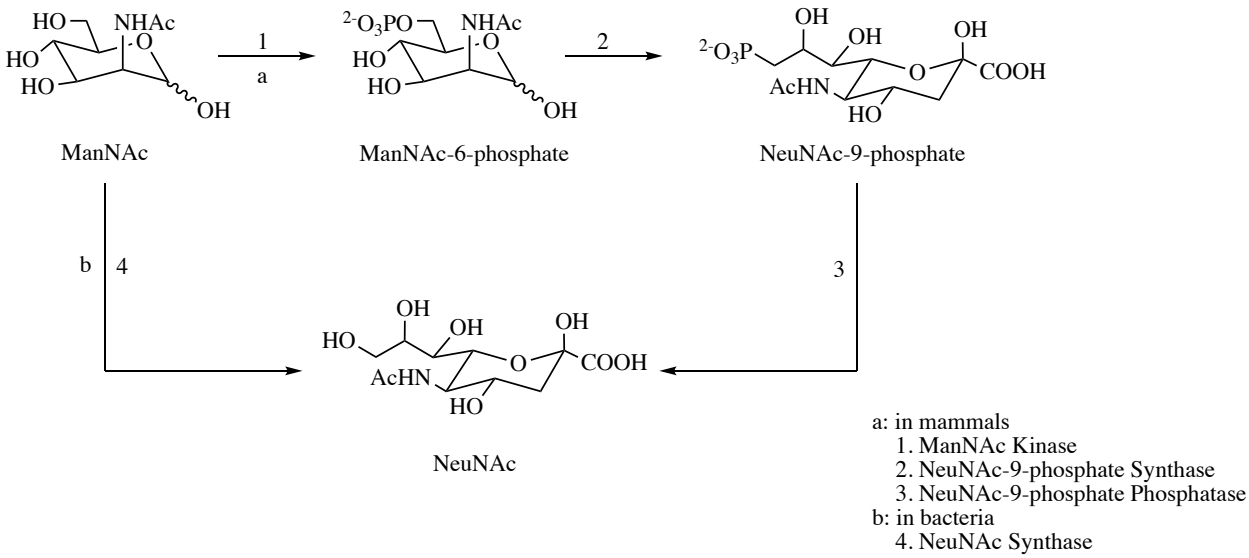

Figure 1.4 Biosynthesis of NeuNAc from ManNAc in mammals and bacteria.

Adapted from reference [43].

1.2.3 KDO8PS

KDO8PS is another α-carboxyketose synthase. It catalyzes the condensation of PEP and A5P to give KDO8P, a precursor to KDO, which is involved in the biosynthesis of lipopolysaccharide (LPS) in Gram-negative bacteria. LPS is located in the outer membrane of Gram-negative bacteria, consisting of a lipid and a polysaccharide chain containing *O*-antigen and core connected by a covalent bond[44]. It is responsible for the toxicity of Gram-negative bacteria and is vital for cell growth. KDO plays a significant role as a link between lipid A, the membrane embedded moiety of LPS[45], and extended polysaccharide molecule *O*-antigen, which is exposed on the outer membrane of bacteria cell and involved in the cellular activity of antibody recognition[44,46] (Figure 1.5). Although the *O*-antigen part in LPS varies from species,

the inner core part containing KDO is highly conserved across all species of Gram-negative bacteria.

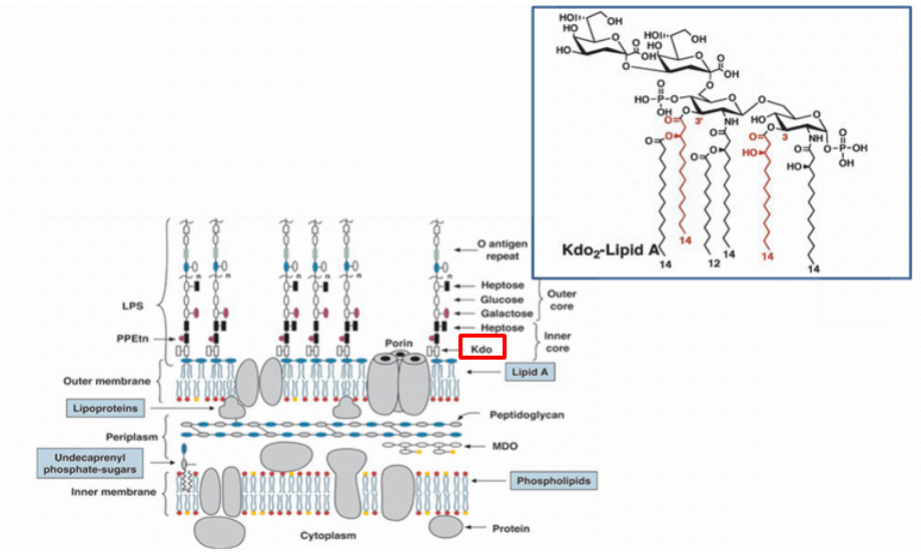

Figure 1.5 LPS structure in Gram-negative bacteria.

Figure taken from Raetz *et al*[44]. The KDO residues are boxed in red.

After the dephosphorylation of KDO8P to KDO, the activated form of KDO, CMP-KDO is formed from CTP and KDO, before it participates into the synthesis of LPS. KDO is essential for the biosynthesis of LPS[47,48]. Mutated KDO8PS in *Salmonella* strains has led to the failure to synthesize KDO, resulting in the inhibition of biosynthesis of LPS and the inhibition of cell growth. As a major component of outer membrane of Gram-negative bacteria, it contributes to the structural integrity of organisms. It also increases the negative charge of the outer membrane which stabilizes the membrane structure[49]. The deficiency in LPS would increase cells' susceptibility to chemical attack. As a result, KDO8PS would be a valuable target for inhibitor design in combatting Gram-negative bacteria.

KDO8PS and DAHPS are homologues[15,50]; however, they have different metal dependencies[51]. All DAHPS are divalent metal-ion dependent, while both metal ions dependent and independent KDO8PS exist[52].

1.3 DAHPS

DAHPS catalyses the first step in shikimate pathway. DAHPSs can be categorized into classes I and II based on sequence homology. Class I DAHPSs are all microbial in origin. They have subunit molecular weights of ~39 kDa, and can be further divided into two subgroups, Iα and Iβ[53]. Type Iα includes DAHPSs from *Escherichia coli*, *Saccharomyces cerevisiae*, and *N. meningitidis*. They possess a regulatory region at their *N*-terminus that inhibits enzymatic activity by combining with Phe, Tyr, and Trp[54]. Type Iβ DAHPS is divided into two types. The first type does not have a feedback regulation domain, while the other type has a feedback regulation domain[54], including chorismate mutase and ferredoxin-like domains located in the *N*-terminus. They regulate the activity of type Iβ DAHPS by downstream amino acids, including Phe, Tyr, Trp, chorismate and prephenate, in independent or cooperative ways[54]. Type Iβ DAHPS shares more similarity with KDO8PS comparing to type Iα DHAPS, and is the most widely distributed DHAPS subtype[53]. Class II DAHPSs were originally found in plants, but have more recently also been found in microorganisms, and have a subunit with molecular weight of 54 kDa[55–57]. There is no significant similarity in the sequence between class I and II DAHPS.

E. coli contains three class Iα isozymes of DAHPS which are feedback inhibited by one each of the aromatic amino acids: DAHPS(Tyr), DAHPS(Phe) and DAHPS(Trp)[58]. Each is negatively regulated by its eponymous aromatic amino acid through feedback inhibition[59,60].

Different feedback regulation mechanisms of class II DAHPS have been reported[28]. Among them, *Mycobacterium tuberculosis* class II enzyme has a complex mechanism of regulatory control. It is inhibited synergistically by the combination of shikimate pathway end products Phe, Tyr, Trp, while Phe, Tyr, or Trp alone only have limited inhibitory effects[20,28,61]. Besides feedback inhibition, another regulatory mechanism found in bacteria is by transcriptional control by the repressor protein *tyrR* and *trpR* which respond to tyrosine and tryptophan levels. Transcriptional control regulation is the only regulatory mechanism found in plants[62].

DAHPSs are divalent metal cation dependent[63]. A variety of divalent metals activate DAHPS *in vitro*, including Mn^{2+}, Fe^{2+}, Co^{2+}, Cu^{2+}, Ni^{2+}, Zn^{2+} and Cd^{2+}. While it is unknown which metal ions function *in vivo*, Fe^{2+}, Zn^{2+} and Cu^{2+} have been proposed[64–66]. It is suggested that the metal ion binds to each monomer of DAHPS[65] and functions as an electrophile to polarize the C1 aldehyde group of E4P for nucleophilic attack by C3 of PEP. It is also believed that it plays a catalytic role in the coordination and orientation of the C1 carbonyl oxygen of E4P[67,68].

1.3.1 DAHPS structure

All DAHPSs share a characteristic $(\beta/\alpha)_8$ TIM-barrel fold and similar active site architecture[59,63,69], and all are either dimeric or tetrameric in solution. *E. coli* DAHPS(Phe) is a homotetramer made up of a dimer-of-dimers in which two subunits form a tightly bound dimer with an extensive inter-subunit interface, and each tight dimer interacts through a weaker interface to form the tetramer (Figure 1.6)[20,67,70]. Each monomer contains a complete active site.

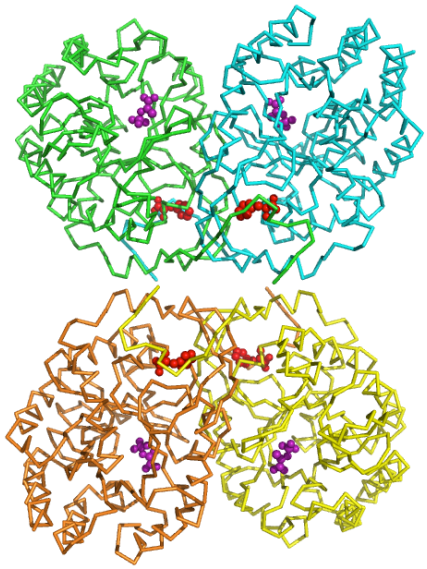

Figure 1.6 The structure of DAHPS(Phe).

DAHPS(Phe) is a homotetramer, each subunit is in different colour. Monomer A (green), B (blue) and C (orange), D (yellow) form two tightly bound dimers through an extensive interface, while dimers AB and CD form a tetramer through a looser interface. There is an active site in each monomer, which is labeled in purple (PEP binding site), while the binding site for its allosteric inhibitor, phenylalanine, is labeled in red. Figure from reference [25].

1.3.2 Catalytic mechanism

DAHPS's condensation reaction of E4P and PEP passes through a tetrahedral intermediate (THI). THI formation is believed to proceed through a cationic transition state or intermediate, though an anionic mechanism has also been proposed[33,67,71]. The cationic mechanism starts with C3 of PEP attacking the carbonyl carbon of E4P, forming the THI, followed by elimination of the phosphate group, producing DAHP (Figure 1.7). In the anionic pathway, the THI is formed through HO^- attacking C2 of PEP. The fact that enolpyruvyl group cannot undergo unactivated nucleophilic attack without prior protonation of the methylene ($C=CH_2$) group[72], and that PEP is base stable argues against the anionic mechanism. THI breakdown involves the breakdown of C-O bond to release P_i and formation of the ketone's double bond (Figure 1.7). Most mechanistic discussions and inhibitor design have focused on

THI formation; however, our recent work on DAHP oxime (see below) suggests that THI breakdown may be the more kinetically significant step.

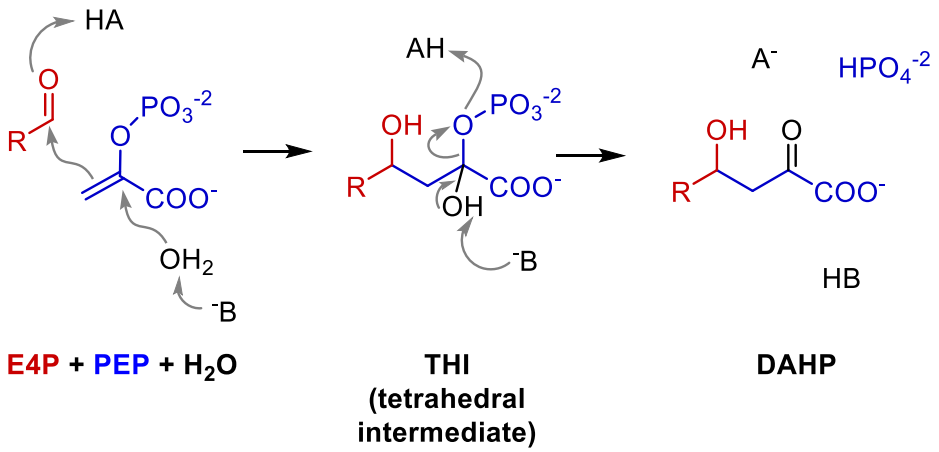

Figure 1.7 The proposed mechanism of DAHPS reaction.

What remains unclear is which mechanism it follows during the THI breakdown. In a cationic mechanism, C-O bond breakage and P_i release happens first, giving a positive charge (blue), while in anionic mechanism, the deprotonation of hydroxyl group happens before the break of C-O bond, which gives a negative charge (red) (Figure 1.8).

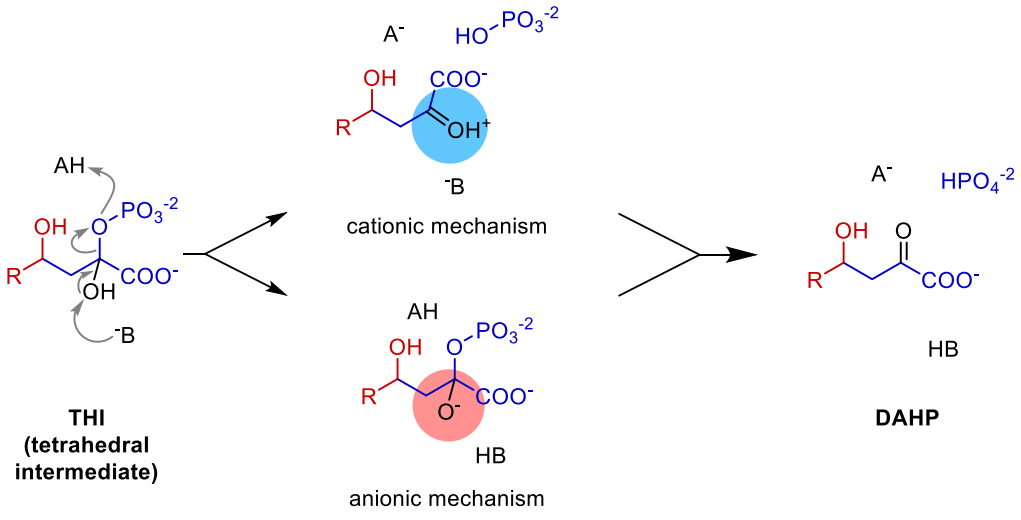

Figure 1.8 Two possible mechanisms of THI breakdown.

Since these two mechanisms give intermediates with opposite charge distributions, knowing which mechanism is operative is a key factor in designing transition state inhibitors. Thus, it is necessary to fully understand DAHPS's catalytic mechanism.

1.3.3 DAHPS inhibitors

Several DAHPS inhibitors have been reported, including the transition state mimic DAHP oxime, which was developed in our lab (Figure 1.9). DAHP oxime is a potent, slow-binding DAHPS inhibitor. It inhibits DAHPS with K_i = 1.5 μM[73]. A linear free energy relationship (LFER) analysis showed that the oxime group not only structurally mimics a phosphate group, but it is also a TS mimic of THI breakdown[74]. This is important because it suggests that the oxime functional group can act as a phosphate mimic in inhibitor design. Phosphate is part of many biomolecules and is involved in most physiological processes, making the development of phosphate mimics a major concern in medicinal chemistry. Phosphate is problematic because it is rapidly hydrolyzed in vivo, and its negative charge makes it cell impermeant. However, designing bioisosteric phosphate replacements remains a challenge because most are either highly charged, leading to problems crossing the cell membrane, or bulky, potentially interfering with its binding with phosphate binding sites[75]. DAHP oxime, as a small uncharged molecule, could be a solution.

A common strategy in inhibitor design is mimicking the reaction intermediates. There is a proposed oxacarbenium ion intermediate in the cationic mechanism during the THI formation. Therefore, oxacarbenium ion intermediate mimics have been developed, such as compound **1** (Figure 1.9). It mimics the positive charge at the carbon atom of the oxacarbenium ion intermediate with IC_{50} = 6.6 μM[76].

Other DAHPS inhibitors include a THI intermediate mimic, compound **2** (Figure 1.9), which replaces the phosphate group in THI with a phosphonate group[77], a substrate E4P mimic, fosmidomycin (Figure 1.9, K_i = 35 μM)[78] , and a PEP mimic, compound **3** (Figure 1.9, K_i = 270 μM)[78]. However, there is no DAHPS inhibitor that is used in clinic.

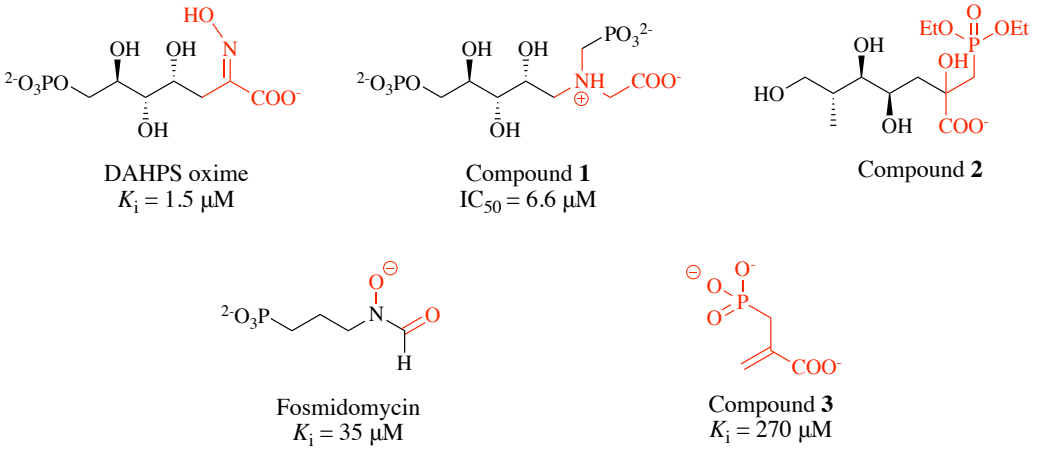

Figure 1.9 DAHPS inhibitors.

Compound **1** is an oxacarbenium ion mimic[76]; **2** is a THI mimic[77]; fosmidomycin in a E4P mimic[78]; **3** is a PEP mimic[78].

1.4 Transition state analysis

Transition state (TS) analysis is a powerful tool for inhibitor design as enzymes bind to and stabilize transition states more than any other species. The dissociation constant of the E·TS complex can be as tight as 10^{-26} M[79], much lower than substrate or product complexes, which typically have dissociation constants in the 10^{-3} to 10^{-6} M range (Figure 1.10).

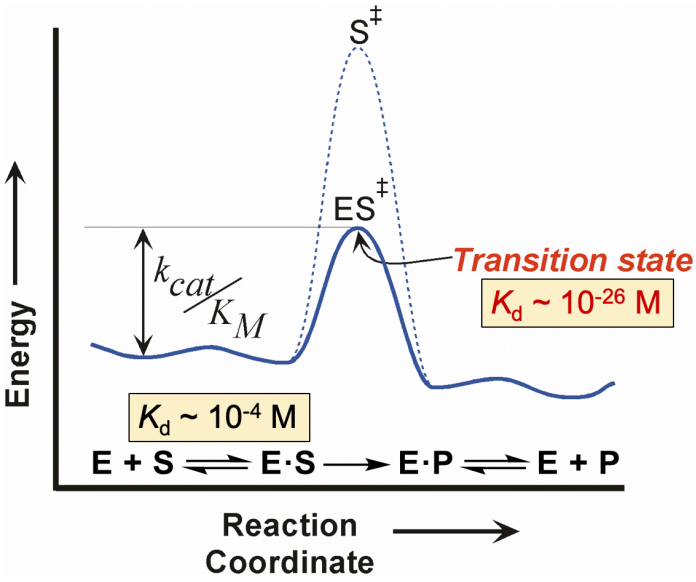

Figure 1.10 E·TS has a much lower dissociation constant than other species.

Enzymes bind their cognate transition states tighter than any other species[79]. Figure by Dr. Berti.

By designing molecules that mimic the transition state's charge and geometry, it is possible to develop potent enzyme inhibitors. Enzyme inhibitors that are TS mimics are used in the clinic include the influenza drugs oseltamivir and zanamivir, the anti-cancer drug pentostatin, the "pril" anti-hypertension drugs, the HIV protease inhibitor saquinavir[80,81], and the anti-T-cell cancer drug forodesine[82,83].

With the information provided by TS analysis, we can get a better understanding of how enzymes catalyze reactions. However, the challenge in studying transition states is their effectively zero concentration, and short lifetimes (10^{-13} s), making it impossible to observe and analyze TS structures using physical or spectroscopic methods[84–87]. The only way to determine TS structures in detail is TS analysis using kinetic isotope effect (KIE) measurements[88,89].

1.4.1 Kinetic isotope effects

A KIE is defined as the ratio of rate constants for a chemical reaction whose reactants contain isotopic labels: KIE = $^{light}k/^{heavy}k$. KIEs are vibrational phenomena and can be explained in terms of a species vibrational frequencies. A bond in a molecule can be treated as a harmonic oscillator, with two masses joined together with a spring (Figure 1.11). The vibrational frequency, ν, is defined by the atoms' masses and the strength of bond (spring) **(**Eq. **1.1**):

$$\nu = \frac{1}{2\pi} \times \sqrt{\frac{k}{\mu}} \qquad \text{(Eq. 1.1)},$$

where k represents the spring's force constant and μ is the reduced mass of the oscillator, $\mu = \frac{m_1 \cdot m_2}{m_1 + m_2}$. Heavier isotopologues have lower vibrational frequencies, and lower frequencies correspond to lower zero-point energies (see below), which give rise to KIEs.

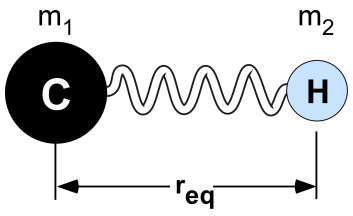

Figure 1.11 Harmonic oscillator model of a C−H bond.

In this harmonic oscillator model of C−H bond, the atoms are treated as balls of mass m_1 and m_2 joined by a spring. At the equilibrium bond length, r_{eq}, the spring exerts no force. As the bond length is changed by Δr, it exerts a force F = −Δrk, where k is the spring's force constant.

Three factors contribute to a KIE: KIE = MMI × ZPE × EXC[90]. MMI is the contribution from the changes in mass and moments of inertia upon isotopic labelling, ZPE is the contribution from zero-point energies, and EXC is the contribution from vibrationally excited states. The ZPE contribution is normally dominant.

1.4.1.1 Zero-point energy

The ZPE contribution arises from changes in the zero-point energies of vibrational frequencies between the reactant and transition state. Zero-point energy is a vibration's energy at 0 K (Eq. **1.2**):

$$E_0 = \frac{1}{2} h \cdot \nu \qquad \text{(Eq. 1.2)},$$

where h is the Planck constant and ν is the vibrational frequency. Because ν depends on the atomic masses and spring force constants, so does E_0. When a bond becomes weaker, i.e., when k decreases, the zero-point energy for the light isotope decreases more than for the heavy isotope, leading to a difference in activation energies, and therefore reaction rates, i.e., an isotope effect.

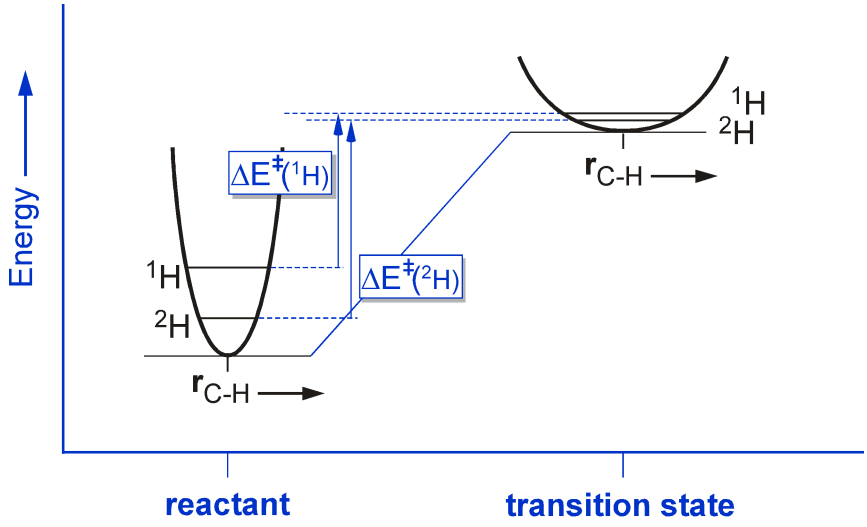

Figure 1.12 Zero-point energy contribution to KIEs

The curves show the energy required to stretch/compress a C–H bond away from its equilibrium bond length, r_{C-H}. Stronger bonds, with higher spring force constants, k, require more energy to distort. The zero-point energy is shown by the horizontal lines. In this example, a C–H bond becomes weaker at the transition state, resulting in the zero-point energy decreasing more for ^1H than ^2H, meaning its activation energy, $\Delta E^{\ddagger}(^1H)$ is lower than ^2H. As a result, ^1H will react faster than ^2H, giving a normal KIE, i.e., KIE > 1.00. Figure taken from reference 88.

1.4.1.2 Classification

KIEs can be classified as primary or secondary. Primary KIEs are those involving the atoms which are undergoing bond breakage or formation, while secondary KIEs are those at any other position in the molecule[88].

KIEs can also be classified as normal (KIE > 1.0) or inverse (KIE < 1.0). A normal KIE demonstrates that the vibrational environment of the labelled atom is looser (i.e., bonding is weaker) in the transition state than that in the reactant, causing the lighter isotopologue to react faster. An inverse KIE demonstrates that the vibrational environment of the labelled atom is tighter, causing the lighter isotopologue to react slower[88].

1.4.1.3 Competitive KIEs

KIEs can be measured noncompetitively or competitively. Non-competitive KIEs involve measuring rate constants for each isotopologue separately. Competitive KIEs involve measuring the ratio of rate constants with both isotopologues present in the reaction mixture at the same time[91]. Competitive KIE measurements yield more accurate and precise results by eliminating systematic error, such as would be introduced by differences in concentration or reaction conditions[92]. Competitive KIEs reflect the isotope effects on the specificity constant, k_{cat}/K_M, in the first irreversible step in the reaction, which depends on the energy of free substrates and free enzymes and of E·TS complex. There is no isotopic discrimination after the first irreversible step[93–95].

1.4.1.4 Measuring KIEs

Measuring competitive KIEs involves measuring the change in isotope ratios as a function of the extent of reaction, which gives, in turn, the ratio of rate constants. Competitive KIEs can be measured using liquid scintillation counting of radioactive isotopes, mass spectrometry, or NMR spectroscopy using stable isotopes[92]. The latter has some advantages over the former; for example, synthesis of substrates with stable isotopes is easier compared to incorporation of radioactive isotopes[96].

Employing NMR to measure ^{2}H KIEs was first reported by Pascal et al. in 1980s[97]. However, these measurements were of relatively low accuracy, and useful KIEs measurements on heavy atoms, like ^{13}C only became possible in the 1990s[98]. These KIEs were measured at natural abundance, which avoided the need for isotopologue synthesis, but required reactions on the multi-mole scale because the low natural abundance of ^{13}C (1%) and ^{2}H (0.02%). In addition, it could not be used for NMR inactive nuclei like ^{18}O. Furthermore, due to the low resolution and sensitivity of early NMR instruments, the accuracy of isotope quantification was limited[96]. Bennet and coauthors developed a direct NMR method to continuously measure competitive KIEs using ^{13}C spectra[92] (Figure 1.13). We plan to use this method to measure ^{18}O KIEs using ^{31}P spectra, something that has not been done before. This method measures the isotope ratio at the site of interest (e.g., ^{16}O/^{18}O) by observing the NMR peaks of an adjacent atom (e.g., ^{31}P). ^{18}O causes a measurable upfield shift in the ^{31}P peak (Figure 1.13A), so that it is possible to quantify the ^{16}O-^{31}P/^{18}O-^{31}P ratio. If the isotopic label at the site of interest is NMR active (e.g., ^{12}C/^{13}C), then the adjacent ^{13}C atom's peak will be split (Figure 1.13B), but the principle is otherwise the same. Using the Bennet method, NMR spectra can be collected continuously as the reaction proceeds until the signal-to-noise ratio becomes too small due to reactant depletion.

This method can avoid the need for large quantities of natural abundance material[99] and the need for an internal reference atom[92], though it does require isotopologue synthesis. Moreover, besides ^{13}C, other NMR-active nuclei can also be used as probes, including ^{15}N and ^{31}P. The main disadvantage of this method is the potential for peak overlap between the reactant and product. The problem of signals overlap can be improved by using a newly developed method, ^{1}H-detected 2D [^{13}C, ^{1}H]-heteronuclear single quantum coherence [HSQC] NMR, reported by Murkin and coauthors[100]. Instead of using ^{13}C as probe, ^{1}H attached to ^{13}C was monitored, which can significantly increase sensitivity [101]. The advantages of this method include small experimental errors, no need for additional sample manipulation, and capability to measure small KIEs. Other KIEs (^{15}N, ^{18}O) can also be measured by this method with the existence of '^{13}C-^{1}H' probe adjacent to the atom of interest[100]. However, not all organic compounds meet with this requirement, which is this method's the major limitation.

(A)

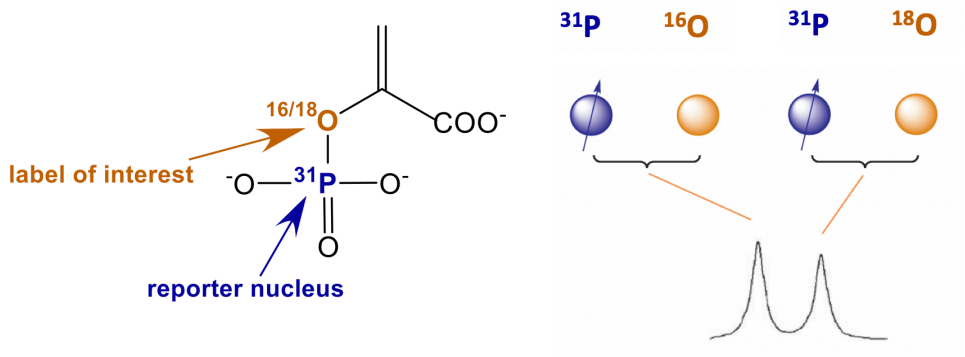

(B)

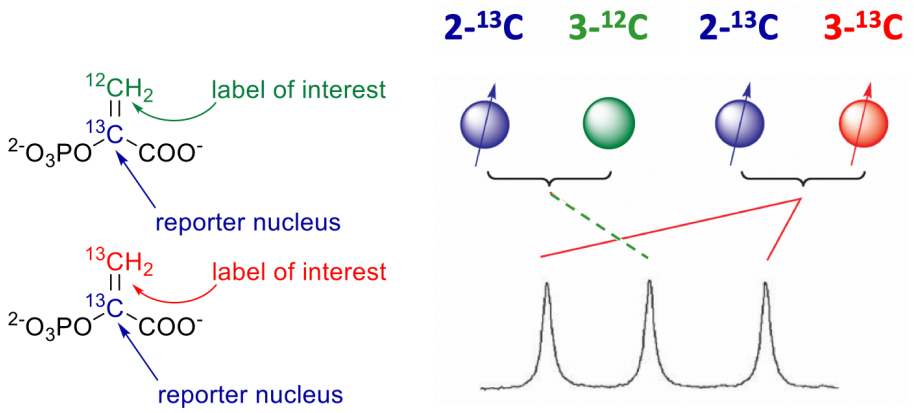

Figure 1.13 Measuring isotope ratios of interest by observing nearby nuclei.

Measuring the isotope ratios of the sites of interest by observing the adjacent reporter nucleus: (a) $^{16}O/^{18}O$ with ^{31}P or (b) $^{12}C/^{13}C$ with ^{31}P NMR has never been used to measure phosphate ^{18}O KIEs before.

KIEs are calculated from the isotope ratios, R/R_0 (Eq. **1.3**):

$$\frac{R}{R_0} = (1 - F_1)^{\frac{1}{KIE}-1} \quad \text{(Eq. 1.3)},$$

where F_1 represents fraction of light isotopologue conversion, R_0 and R represent the ratio of heavy to light isotopologue before and after reaction, respectively.

1.4.2 Solving transition state structures

Once experimental KIEs have been measured, the next step is to interpret them to solve the TS structure. There is no route to calculate a TS structure directly from experimental KIEs. Instead, because it is possible to reliably predict what the KIEs would be for a candidate TS structure from its vibrational frequencies, calculated KIEs are generated for multiple candidate TS structures[88]. The candidate TS structure whose calculated KIEs matches the experimental values is considered the experimental TS structure.[88,102]

1.5 Quantitative NMR

NMR is frequently considered a non-quantitative technique, in large part because the most commonly used conditions are optimized for sensitivity at the expense of quantification. Nonetheless, NMR can be used for quantitative analysis[103], and has been since 1963, when Hollis[104] performed the first quantitative NMR (qNMR) measurement on a mixture of drugs to analyse the fraction of each compound. NMR is uniquely suitable for the analysis of mixtures because of its non-selective characteristic[105]. That is, it is able to simultaneously detect all compounds which contain the nucleus under observation. Despite these advantages, its application to some nuclei, such as ^{31}P and ^{13}C, is limited due to their low sensitivity (^{31}P) or low natural abundance (^{13}C). However, the development made in high-field magnets, cryoprobes[106–109], solvent suppression techniques[110], and versatile pulse sequences have decreased its limit of detection (LOD) significantly.

The precision and accuracy (higher than 98%) of qNMR have been validated to be comparable to those of HPLC[111], while requiring relatively short analysis times. However, the precision and accuracy can only be achieved after taking careful considerations regarding acquisition and processing parameters. It also needs efforts in sample preparation, which may also introduce significant errors.

The most fundamental principle of qNMR is based on the relationship between signal intensity (I) and number of nuclei (N) (Eq. **1.4**):

$$I = Ks \cdot N \qquad \text{(Eq. 1.4)},$$

where Ks represents the spectrometer constant. The intensity I of a signal is directly proportional to the number of nuclei N [103,111]. Under the right conditions, qNMR can be used for

relative quantification of two species in a solution, or absolute quantification by using an external standard[111,112]. The molar ratio of two substances (*X* and *Y*) can be determined by the comparison of normalized intensities of corresponding signals[112], and can be calculated directly (Eq. **1.5**)

$$\frac{n_X}{n_Y} = \frac{I_X}{I_Y} \cdot \frac{N_Y}{N_X} \qquad \text{(Eq. 1.5)},$$

where n_n is molar ratio, I_n is the integral area, and N_n is the number of nuclei[113,114].

1.5.1.1 The NMR signal

NMR spectra are generated by placing the sample in a magnetic field and applying a radiofrequency (*rf*) pulse to the nucleus of interest, causing its magnetic moment to flip by 90° from the z-axis to the x-y plane[98] (Figure 1.14). The magnetic moment precesses in the magnetic field, and this precession is detected by the spectrometer as the free induction decay (FID). FID is the observable sinusoidal signal (signal versus time) generated by the transverse component of the non-equilibrated magnetization as it precesses in the x-y plane. The FID cannot be interpreted directly; a Fourier transform (FT) is applied to convert the time domain FID to a frequency domain NMR spectrum.

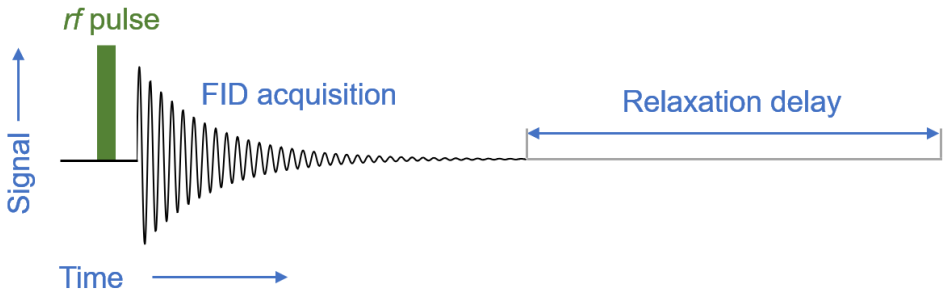

Figure 1.14 NMR single pulse and FID.

1.5.1.2 Relaxation

Relaxation time is an important factor in the accuracy of qNMR. FIDs decay over time through two modes as the magnetic moment relaxes, namely longitudinal and transverse relaxation (Figure 1.15).

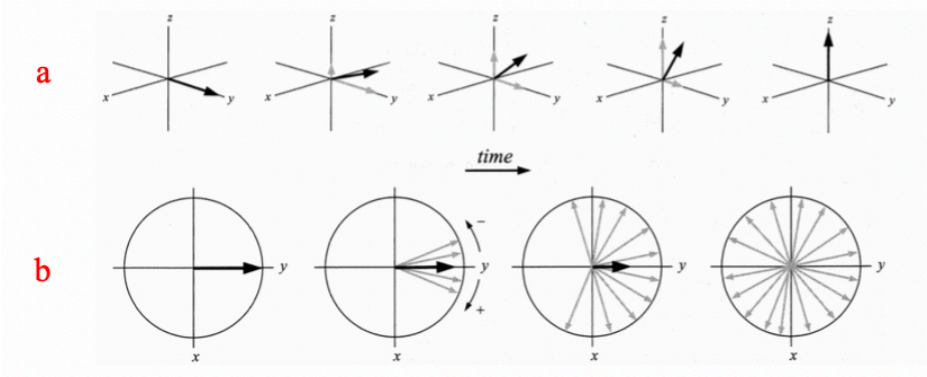

Figure 1.15 Spin Relaxation.

(a) Longitudinal relaxation. Immediately after the *rf* pulse, magnetization is in the x-y plane. Over time, the magnetization returns to its maximum value along +z axis. (b) Transverse relaxation, in which slight differences in precession frequency cause the magnetic vectors to become dispersed in the x-y plane, leading to a decrease in the magnetization vector[115]. Figure taken from reference 115.

Relaxation is a process by which the nucleus's magnetization returns to its initial value along the z-axis at its equilibrium state. Transverse relaxation is faster than longitudinal relaxation, and since NMR peak widths are inversely proportional to relaxation time, T_2 determines the peak width. In practice, it is faster to measure T_2*, the "effective T_2"[115], which includes contributions from the molecule's intrinsic T_2 value, and a small contribution from magnetic inhomogeneity in the NMR instrument, $T_{2(\Delta B0)}$ (Eq. **1.6**):

$$\frac{1}{T_2^*} = \frac{1}{T_2} + \frac{1}{T_{2(\Delta B_0)}} \qquad \textbf{(Eq. 1.6)},$$

In this study T_2* was measured as a proxy for T_2.

Longitudinal relaxation always takes longer than transverse relaxation, so it is the relaxation mode that must be considered during qNMR. Longitudinal relaxation is a simple exponential process with T_1 as a first-order time constant (Eq. **1.7**):

$$M_z = M_0\left(1 - e^{-\frac{t}{T_1}}\right) \quad \text{(Eq. 1.7)},$$

where M_0 is the magnetization at thermal equilibrium, and M_z is the magnetization along the z-axis at time, t.

T_1 can be measured using inversion recovery method[115–117](Figure 1.16). A 180° pulse is applied, followed by a variable delay period, τ. Longitudinal relaxation begins during the delay period, then another 90° pulse is applied. The strength of the signal depends on amount of longitudinal relaxation during τ. For example, when $\tau = T_1$, the second pulse will flip the magnetic moment back to 180°, and there will be no observable signal during the FID. The experiment is repeated with varying t_1 value from a small value to at least $7 \times T_1$. A plot of peak intensities versus τ gives value of T_1[118].

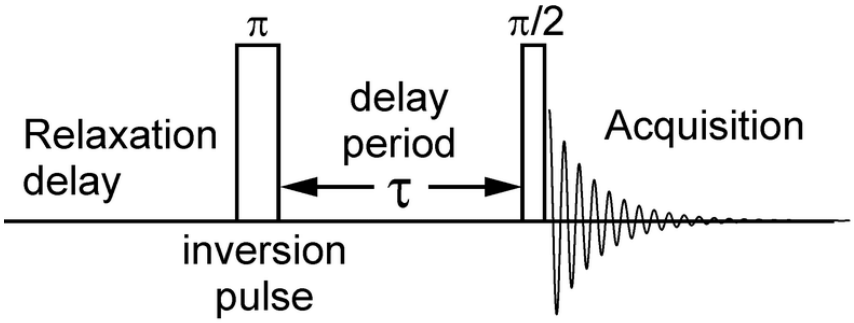

Figure 1.16 Pulse sequence of inversion-recovery pulse for measurement of T_1 relaxation time constant.

Figure taken from reference[119].

NMR spectra will be quantitative only if the magnetic vector is allowed to fully relax between each *rf* pulse. If a pulse is applied before the nuclear spins are completely relaxed, then each nucleus with a different T_1 value will flip to a different angle and give a different strength signal. Full relaxation can take minutes, which makes quantitative measurements extremely time consuming. For qNMR, relaxation times of $7 \times T_1$ are required.

Traditionally, the only way to speed data acquisition for qNMR was to use NMR relaxation agents, such as paramagnetic ions like Gd^{3+} or Eu^{3+}, to accelerate the relaxation process[120]. In this thesis, we investigate a second approach, namely using incomplete T_1 relaxation. The rationale was that isotopic labels (^{16}O, ^{18}O) are unlikely to affect T_1 values at the adjacent ^{31}P nucleus, so even if a ^{31}P nucleus is not completely relaxed, the effect would be the same for ^{16}O-^{31}P versus ^{18}O-^{31}P, and the isotope ratio would be accurate even without full longitudinal relaxation. This rationale was proposed by Prof. Andrew Murkin (U. Buffalo) and is supported by NMR theory, which states that a steady state condition should be established after a handful of pulses[121,122]. A stable, steady state should allow accurate isotope ratios to be measured.

The excitation pulse should be uniform throughout the whole spectral width of interest. It requires short pulses (~10 μs). It is easier to achieve for proton NMR, but for heavier nuclei with a larger chemical shift range, such as ^{19}F or ^{31}P, the spectra may suffer from intensity distortions. Normally, the maximum intensity can be achieved by applying a 90° pulse, but this always requires longer relaxation time. A smaller pulse angle can also be used to achieve robust signal-to-noise (S/N) ratio with shorter time, which is known as 'Ernst angle', α [123–125] (Eq. **1.8**):

$$\cos\alpha = e^{\left(-\frac{T_R}{T_1}\right)} \qquad \text{(Eq. } \mathbf{1.8}\text{)},$$

where α represents the optimum pulse angle, and T_R, T_1 represent repetition time and relaxation time respectively.

1.5.1.3 Relaxation agents

As mentioned above, a time delay of $7 \times T_1$ is needed between each pulse for complete relaxation, and for [1-^{13}C]pyruvate, its T_1 is longer than 10s. Thus, it is necessary to wait for more than 1 minute for full recovery, which makes measurement quite long. Under these conditions, relaxation agents (also called contrast agents) can be used to reduce T_1, thereby speeding data acquisition. Relaxation agents are paramagnetic species, such as gadolinium chloride, the most commonly used for aqueous solutions[126–128]. Paramagnetic agents reducing relaxation time can be explained by dipolar-dipolar interaction mechanism. A spin-1/2 nucleus (such as ^{13}C or ^{31}P) can be seen as a 'magnet' which possesses a magnetic 'North' and 'South' pole, and as two such dipoles approach to each other, their associated magnetic field interact. So, for two neighboring nuclei in a molecule that is tumbling in solution, the local field experienced at one of these nuclei will fluctuate as its neighboring nuclei tumbles in solution. As a result, relaxation can be induced when the tumbling rate is close to Larmor frequency[129–132]. The magnetic moment of an unpaired electron is about 660 times of that of the proton, so it provides a very efficient relaxation resource[133]. Gadolinium is a powerful relaxation agent due to its unique electric structure. It has 7 unpaired electrons in its 4f shell, accounting for its ability of reducing relaxation time. These unpaired electrons are not involved in ionic bonding to chelators, so this ability is retained even when chelated to a ligand such as deferoxamine B (DFO)[130], a chelating agent. Relaxation agents reducing relaxation time is concentration dependent, and the empirical relationship between [Gd^{3+}] and T_1 is given by (Eq. **1.9**):

$$T_1 = (T_{1,0} - T_{1,\text{inf}}) \times e^{-\frac{[Gd]}{k}} + T_{1,inf} \quad \text{(Eq. 1.9)},$$

where $T_{1,0}$ is the T_1 relaxation time when no relaxation agent is added, $T_{1,\text{inf}}$ is the lowest possible T_1 relaxation time at infinite Gd concentration, and k is the concentration dependence. From this equation, T_1 approaches $T_{1,\text{inf}}$ when $[Gd^{3+}]$ is $> 5 \times k$. This suggests that one of these 2 parameters are when required when measuring KIEs: (1) $[Gd^{3+}]$ used is 5 times of concentration dependence; or (2) delay time is $7 \times T_{1,0}$.

1.5.1.4 Signal-to-noise ratio

The signal-to-noise ratio (S/N) is a significant factor in accurate peak integrations and measurements. Acquisition and processing parameters need to be optimal to ensure an accurate analysis, which requires S/N of the resonances of interest to be at least 100 in absolute quantitation and be at least 20 in relative quantitation. S/N is proportional to the square root of the number of scans and increases with the strength of the applied magnetic field, B_0, as $B_0^{\frac{3}{2}}$ [134]. A traditional way to increase S/N is to increase the number of scans but doubling the S/N requires quadrupling the number of scans, which can be prohibitive for some applications[135].

Other factors that affect S/N include the probe and receiver. Probe availability and tube configuration can have a bigger impact on S/N than the size of the magnet. For example, a 3mm probe can improve S/N up to 50% compared to a 5mm probe[136]. Moreover, the development of cryoprobe also greatly improves the S/N.

1.5.1.5 Integration and deconvolution

Numerical integration is performed by defining a peak of interest and summing the intensity at each point in the region of interest. Accurate integration requires satisfying a number of criteria, including separation of the peaks of interest by at least 20 × the line width. This amount of separation is not possible in this study. Instead, peak deconvolution is used. Deconvolution involves fitting the experimental spectrum to a defined peak shape, then using the fitted values of peak height and width to analytically calculate the peak area. The main advantage of peak deconvolution is the ability to use it with overlapping peaks. Ideally, liquid NMR resonances have a Lorentzian shape, but practically, this is difficult to achieve as the NMR spectrometer itself also contributes to the peak shape. The spectrometer's contribution has a Gaussian peak shape. Under this circumstance, Voigt deconvolution, that is, a mixed Lorentzian-Gaussian peak shaping function, is commonly used to fit peaks, especially for those asymmetrical peaks caused by poor shimming[137,138].

1.6 Hypothesis

The goal of this thesis was to measure the [2-^{18}O]PEP KIE for the DAHPS-catalyzed reaction. Given the evidence that the first irreversible transition state of the reaction is THI breakdown[74], a large normal ^{18}O-KIE (> 1.0) would be expected when the breakdown of THI follows the cationic mechanism, since the vibrational environment of ^{18}O is looser because of the break of C-^{18}O bond. An anionic mechanism of THI breakdown would be expected to give a ^{18}O-KIE of unity, as the vibrational environment of ^{18}O does not change during the reaction.

2 ***Materials and Methods***

2.1 General

His_6-tagged *E. coli* DAHPS(F) (DAHPS) was expressed and purified as described previously[25]. DAHPS initial velocity measurements were made the colorimetric Malachite Green/ammonium molybdate (MG/AM) assay to detect inorganic phosphate (P_i) released by DAHPS[139]. All substrate solutions and buffers, with the exception of the enzyme and $MnCl_2$, were treated with Chelex 100 to remove contaminating metal ions. All enzymatic reactions were performed at 25 °C. ^{18}O-water was from Cambridge Isotope Labs, and all other reagents were from Sigma-Aldrich or Bioshop (Burlington, ON), unless otherwise stated.

2.2 Purification of the PEP synthetase ppsA

The pET24b expression plasmid for PEP synthetase (ppsA) was a gift from Prof. David Jakeman (Dalhousie University). The plasmid was transformed into *E. coli* BL21 electro-competent cells by electroporation and plated on 50 μg/mL kanamycin-agar plate for incubation overnight at 37 °C. A single colony was picked and inoculated into 50 mL of lysogeny broth (LB) medium with 50 μg/mL kanamycin , and was incubated overnight at 37 °C. The 50 mL overnight culture was sub-cultured into 1 L LB medium containing 50 μg/mL kanamycin and grown with shaking at 37 °C to OD_{600} = 0.8. Overexpression was induced by 0.2 mM isopropyl β-D-1-thiogalactopyranoside (IPTG), followed by overnight incubation at 17 °C. Cells was harvested by centrifugation at 10000 × g for 20 min. Cells were homogenized in 5 mL/gram of cell of Buffer A (25 mM imidazole, 20 mM Tris-Cl, pH 8.0, 0.3 M NaCl). Cells were then lysed in a Constant Systems cell disruptor at 20,000 psi. Cell debris were removed by centrifugation at 10000 × g for 30 min and the supernatant was filtered at 0.45 μm and was loaded onto a 1 mL

Ni^{2+}-loaded Hi-Trap chelating column (GE Healthcare). The column was washed with 10 column volumes of wash Buffer A, then ppsA was eluted with Buffer B (250 mM imidazole, 20 mM Tris-Cl, pH 8.0, 0.3 M NaCl). The protein was homogenous based on SDS-PAGE electrophoresis. The purified protein was dialyzed against dialysis buffer (1 mM EDTA, 1 mM dithiothreitol (DTT), 50 mM Tris-Cl, pH 8.0, 5% (v/v) glycerol) for 48 h. The concentration of ppsA was determined using the Edelhoch method, using ε_{280} = 69 720 M^{-1} cm^{-1}. The purified protein was flash frozen and stored at -80 °C.

2.3 Substrates synthesis and purification

2.3.1 PEP

PEP was synthesized by dissolving 30 mM ATP, 20 mM sodium pyruvate, and 20 mM $MgCl_2$ in 400 mM Tris–Cl, pH 8.4, at room temperature, with a final volume of 2 mL. The reaction was started by adding 100 µL of purified ppsA. The pH was monitored, and 0.5 M NaOH was added as necessary to maintain pH 8.0. Another 100 µL of ppsA was added after 2 h. After 4 h, the reaction was stopped by heating at 94 °C for 5 min. The precipitated protein was removed by centrifugation. The lactate dehydrogenase (LDH) assay and pyruvate kinase (PK) assays were used to determine the residual pyruvate and PEP concentrations, respectively, to calculate the yield.

The PEP synthesis mixture was injected onto two C-18 reverse phase chromatography columns connected in series (7.8 x 300 mm, 15 µm particle size, 300 Å pore size, Waters), and eluted with 25 mM *N, N*-diisopropylethylamine (DIEA) acetate, pH 6.2, at a flow rate of 2 mL/min and absorbance detection at 230 nm. PEP eluted around 30 min. The collected PEP was concentrated to 2 mL by rotary evaporation and injected onto a 20 mL SP-Sepharose (GE Life

Sciences) cation exchange column that was previously charged with H^+ with 1 M HCl, and eluted with ddH_2O at a flow rate of 2 mL/min to remove DIEA cations. After overnight lyophilization, PEP was identified by ^{1}H-NMR.

2.3.2 ^{13}C-PEP

^{13}C-labelled PEP was synthesized using the same method as above, using ^{13}C-labelled sodium pyruvate as starting material. The lactate dehydrogenase (LDH) assay and pyruvate kinase (PK) assays were employed to calculate the yield.

Table 2.1 The starting material used in the synthesis of 13C-labelled PEP.

Starting material	Product
[2-^{13}C] sodium pyruvate	[2-^{13}C] PEP
[3-^{13}C] sodium pyruvate	[3-^{13}C] PEP
[2,3-^{13}C] sodium pyruvate	[2,3-^{13}C] PEP

^{13}C-labelled PEP was purified using the same method as above and was identified by both ^{1}H-NMR and ^{13}C-NMR.

2.3.3 [2-^{18}O]PEP

[2-^{18}O]PEP was synthesized using the same method as above in 50% $H_2{}^{18}O$. $H_2{}^{18}O$ was recovered after the reaction by lyophilization. The reaction mixture was re-dissolved in 1 mL ddH_2O. The ppsA was precipitated by heating the reaction mixture at 94 °C for 5 min and removed by centrifugation. The lactate dehydrogenase (LDH) assay and pyruvate kinase (PK) assays were employed to calculate the yield. [2-^{18}O]PEP was purified as above and was identified by both mass spectrometry and ^{31}P-NMR.

2.3.4 E4P

Erythrose 4-phosphate (E4P) was synthesized by the oxidative degradation of glucose 6-phosphate (G6P) using lead tetraacetate based on the method by Sieben et al.[140], and modified by Balachandran[25]. G6P (200 μmol) was dissolved in 50 mL of acetic acid and lead tetraacetate ($Pb(OAc)_4$, 400 μmol) was dissolved in 12 mL of acetic acid containing 420 μmol of H_2SO_4. G6P was titrated with 500 μL aliquots of lead tetraacetate every minute. The reaction was monitored by starch-iodide testing paper which turns purple in the presence of Pb^{4+} due to it oxidizing I^- to I_2, which then forms a coloured complex with starch. The testing paper was made by adding 2.5 g starch into 250 mL boiled water, and adding 0.5 g sodium iodide when it was cool. The paper was dipped and dried. When the testing paper showed a purple colour that did not fade within 5 min, that indicated that all the G6P had been consumed. An additional 10 μmol of G6P was then added to consume the residual $Pb(OAc)_4$ to avoid over-oxidation of E4P to glyceraldehyde 3-phosphate , a DAHPS inhibitor. The solution was filtered through a Celite filter and the Celite was washed with 100 mL water. The flow-through was concentrated under vacuum to a volume of 15mL at 5 °C. The half sample was purified on a 5 mL Q-Sepharose column, and eluted with a gradient from 95% Buffer A (10 mM ammonium bicarbonate, pH 6.2), and 5% Buffer B (10 mM ammonium bicarbonate, pH 6.2, 2 M sodium formate) to 60% Buffer A and 40% Buffer B over 30 min. The eluent was collected in 30 vials, and examined by reducing sugar assay, G6P dehydrogenase assay and DAHPS enzymatic assay. The vials of E4P that were confirmed in assays were pooled and concentrated to 5 mL under high vacuum. The collected E4P was run through 20 mL SP-Sepharose (GE Healthcare) cation exchange column charged with HCl to remove ammonium ions and Pb^{2+} and eluted with ddH_2O. E4P was lyophilized under high vacuum to a volume of 10 mL and stored at -20 °C.

2.4 Substrates quantification

2.4.1 PEP

The synthesized PEP was quantified by a coupled spectrophotometric enzymatic assay in which pyruvate and PEP were both quantified. Pyruvate was quantified by reduction to lactate by LDH, with a concomitant oxidation of NADH to NAD^+ ($\Delta\varepsilon_{340}$ = 6220 M^{-1} cm^{-1}). PEP was quantified by pyruvate kinase, which converts PEP and ADP to pyruvate and ATP. Pyruvate is then consumed by LDH as above. A 3 mL assay mixture containing 100 µL of ppsA reaction mixture, 100 µL of 45 µM ADP, 100 µL of 66 µM NADH and 2.7 mL LDH/PK assay buffer (0.05 M Tris-HCl, pH 7.6, 0.12 M KCl, and 0.062 M $MgSO_4$) was prepared. A 1 mL aliquot of assay mixture was added into a cuvette and A_{340} monitored. LDH (10 U) was added when the baseline was stable and A_{340} was monitored until it was stable again. Pyruvate kinase (5 U) was then added and A_{340} monitored again until it was stable. A_{340} decreased as NADH was converted to NAD^+. The concentration of residual sodium pyruvate and synthesized PEP are given by the equation:

$$C = \frac{\Delta A_{340}}{\Delta \varepsilon_{340}} \times \frac{V_1}{V_2}$$

where ΔA_{340} is the change of absorbance after adding each enzyme, $\Delta\varepsilon_{340}$ is the change in extinction coefficient upon NADH oxidation, V_1 is the total volume of assay mixture, and V_2 is the total volume of ppsA reaction mixture added.

2.4.2 E4P

2.4.2.1 Reducing Sugar Assay

The reducing sugar assay measures the concentration of an aldehyde sugar, in our case, E4P, by the detecting the reduction of Cu^{2+} to Cu^{+} by the latter's ability to form a coloured complex with 2,9-dimethyl-1,10-phenanthroline (neocuproine)[141]. Glucose standards were prepared by adding 0 – 100 µL of 1 mM glucose into a 375 µL solution containing 187.5 µL of solution A (4% Na_2CO_3 , 1.6% glycine, 0.045% anhydrous $CuSO_4$) and 187.5 µL of solution B (0.12% 2,9 -dimethyl -1,10-phenanthroline), then bringing the total volume to 1 mL with ddH_2O. The sample assay solution was prepared with 10 µL of E4P sample solution, 187.5 µL solution A, 187.5 µL of solution B, and 615 µL of ddH_2O. The solution was heated at 95 °C for 8 min and the A_{450} was read.

2.4.2.2 DAHPS enzymatic assay

E4P was quantified with DAHPS enzymatic assay using varying volumes of E4P sample in the reaction mixture. Reaction mixtures containing 5 mM PEP, 20 µM $CdCl_2$ and varying volumes of E4P were brought to a total volume of 200 µL with 50 mM K-HEPES, pH 7.6, 100 µM TCEP. The reaction was started by adding 20 nM DAHPS and run to completion for 30 min. The amount of E4P was calculated by monitoring the product P_i using the MG/AM assay.

2.5 DAHPS kinetics assay

All initial velocities (v_0) were measured using by following inorganic phosphate (P_i) production using the MG/AM assay. All buffers and substrates, except $CdCl_2$, were treated with Chelex 100 (Bio-Rad Laboratories, Inc.) prior to use, to remove residual divalent metal ions.

The assay was started by adding 20 nM DAHPS into a total volume of 200 μL reaction mixture of 100 μM PEP, 100 μM E4P, 100 μM TCEP, 50 mM HEPES pH 7.6, and varying concentrations of Cd^{2+} (pH of the reaction mixture was adjusted to 8 with 1 M NaOH). Aliquots of 20 μL were taken every 60 s from the reaction mixture and added into a 96-well plate well containing 50 μL MG/AM solution and 30 μL ddH_2O, which was then quenched by adding 10 μL 34% citrate after 90 s. The reaction took place at 30 °C.

2.6 NMR acquisition

2.6.1 T_1 measurement

The longitudinal relaxation times (T_1) of ^{13}C and ^{31}P were measured using the inversion recovery method. T_1 was calculated using the built-in dynamics function of the program TopSpin (Bruker). T_1s were measured under a variety of conditions, including varying concentration of $GdCl_3$, sample treatment with Chelex 100 and/or degassing (i.e., deoxygenation) and at different spectrometry frequencies. The empirical relationship between Gd^{3+} concentration and T_1 is given by (Eq. **1.9**.

2.7 NMR processing

$^{16}O/^{18}O$ ratios in ^{18}O-labelled P_i and PEP were quantified by ^{31}P NMR, with ^{16}O and ^{18}O giving slightly different ^{31}P chemical shifts. NMR spectra for peak deconvolution were processed with TopSpin by applying exponential multiplication (efp) with zero filling (SI) to 512k points and line broadening (lb) of 1 Hz. The overlapped peaks were initially deconvolved using TopSpin's built-in Lorentzian-Gaussian deconvolution function. However, the lack of adjustable fitting parameters made it less trustworthy. So, another peak-fitting program, Peakfit

(Systat Software, Inc.) was used. Two different models of deconvolution were tested, namely Lorentzian and Voigt deconvolution[142]. Lorentzian gives the "natural" peak shape of NMR spectra, while Voigt deconvolution includes a combination of Lorentzian (natural peak shape) and Gaussian (instrument contributions) deconvolution[115]. The ratio of $^{16}O/^{18}O$ was calculated by the ratio of peak area of respective peaks using each deconvolution model.

2.8 Standard curves of isotope ratio

2.8.1 ^{18}O-labelled phosphoric acid

Phosphoric acid was labelled by exchange with $H_2{}^{18}O$. A mixture of 45 µL of 320 mM phosphoric acid and 15 µL of $H_2{}^{18}O$ (99%) was sealed in a 200 µL crimp vial and heated at 120 °C for 3 days[143]. The reaction mixture was cooled to room temperature and quenched by adjusting the pH to neutral using NaOH.

2.8.2 Measurement of isotope ratio

The $^{16}O/^{18}O$ isotope ratio was calculated by the ratio of respective NMR peak areas. The ^{31}P-NMR spectra were obtained using proton decoupled ^{31}P-NMR using 600 MHz NMR under two different acquisition conditions (Table 2.2) and processed as described above.

Table 2.2 Two acquisition conditions of 31P-NMR for measuring isotope ratio.

Condition	Flip angle	Number of pulses	SW (ppm)	O1P (ppm)	Repetition time (s)	Acquisition Time (h)
1	90°	200	33	0	119	6.0
2	30°	600	33	0	3.5	0.7

2.8.3 Standard curve of isotope ratios

The accuracy, precision and linearity of the measurement of the $^{16}O/^{18}O$ in ^{18}O-labelled was assessed by measuring the $^{16}O/^{18}O$ ratio in labelled P_i, then adding aliquots of unlabelled phosphoric acid. In a typical experiment, the $^{16}O/^{18}O$ ratio was measured as described above for a 600 µL sample of 15 mM phosphate on the 600 MHz NMR spectrometer. Aliquots of 1 mol% each of unlabelled phosphoric acid were added and the $^{16}O/^{18}O$ ratio measurement was repeated.

3 Results

3.1 Purification of ppsA

The first attempt to express ppsA failed. Sequencing the plasmid showed that the stop codon was mutated, leading to a too-long sequence. Site-directed mutagenesis was employed to acquire the correct plasmid. ppsA was then successfully expressed and purified using nickel affinity chromatography. The purity was verified by SDS/PAGE (Figure 3.1). ppsA was stable for months at -80 °C.

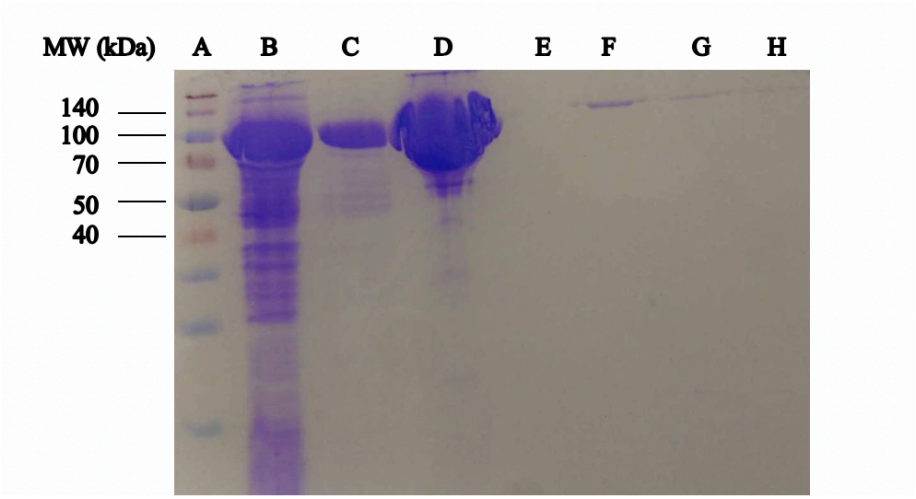

Figure 3.1 10% SDS-PAGE of ppsA.

Lane A: protein ladder; Lane B: column flow-through; Lane C: column wash with Buffer A; Lane D-H: column elution fractions 1-5.

3.2 Purification of DAHPS

N-terminally His_6-tagged DAHPS ($DAHPS_{H6}$) was purified using nickel affinity chromatography. The purity was verified by SDS/PAGE (Figure 3.2). $DAHPS_{H6}$ was stable for months at -80 °C.

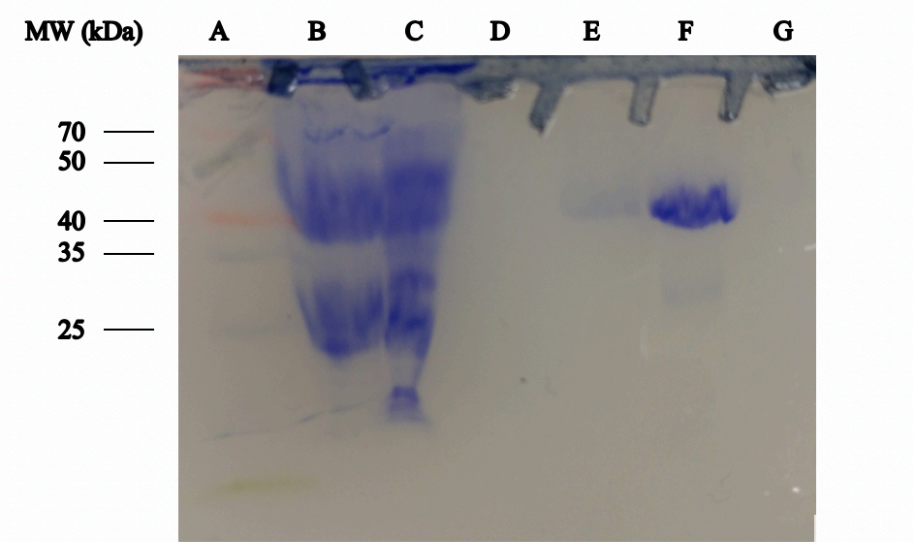

Figure 3.2 10% SDS-PAGE of DAHPS (Phe).

Lane A: protein ladder; Lane B: cell lysate; Lane C: column flow-through; Lane D: column wash with 10% Buffer B; Lane E: column wash with 10% Buffer B; Lane F: column elution with 80% buffer B; Lane G: column wash with 100% Buffer B.

3.3 Substrates synthesis and quantification

3.3.1 PEP

In the past, our lab has used anion exchange to purify PEP, DAHP, and related anionic small molecules. A significant drawback of this method is that the purified molecule elutes in a strong salt solution, roughly 300 mM ammonium formate. In principle, the salt is volatile and

can be removed by lyophilization. In practice, it takes 1 to 2 weeks of repeated cycles of dilution and lyophilization to reduce the salt concentration enough to be used in rate assays. It is an even larger problem for NMR, where the high ionic strength leads to broad peaks and sample heating. Instead, a new ion-paired reverse phase HPLC method was developed to purify PEP. *N, N*-diisopropylethylammonium acetate (DIEAA) was used as the ion pairing agent. The hydrophobic amine ion pairs with PEP's three negative charges, making PEP effectively more hydrophobic and increasing its retention time on the C18 column (T_R = 30 min). Repeatedly lyophilizing DIEAA did not remove all the amine, so a cation exchange chromatographic step was used to remove amine ion. The purified PEP was verified by ^{1}H-NMR (Figure 3.3).

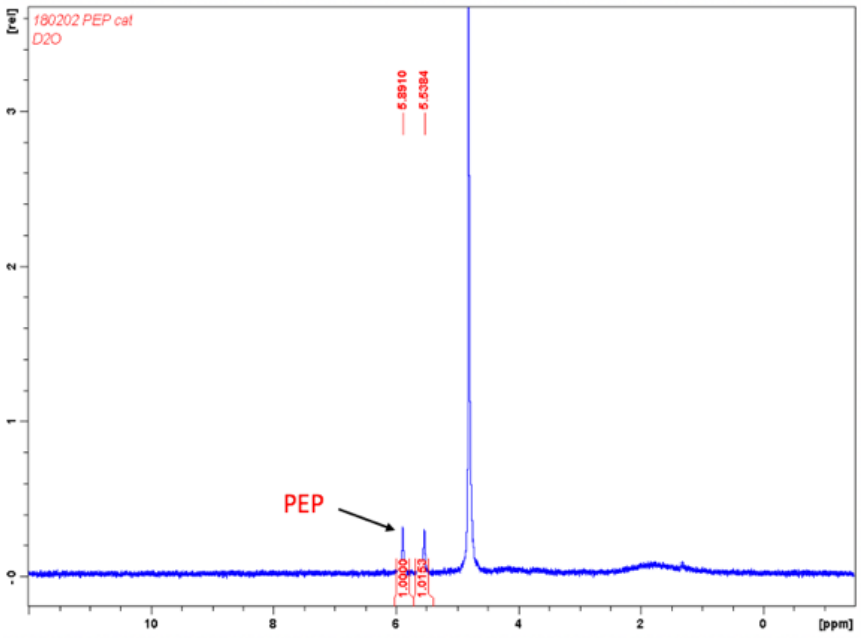

Figure 3.3 ^{1}H-NMR spectra of overnight lyophilized PEP.

Chemical shift: ^{1}H (*s*, 5.54 ppm) and ^{1}H (*s*, 5.89 ppm). The peak at 4.8 ppm is HOD.

3.3.2 *^{13}C-PEP*

For the measurement of ^{13}C KIEs, singly and doubly labeled ^{13}C PEP were synthesized from ^{13}C sodium pyruvate. The purification method was the same as mentioned above. The purified ^{13}C PEP was verified by both ^{1}H-NMR (data not shown) and ^{13}C-NMR (Figure 3.4).

(A)

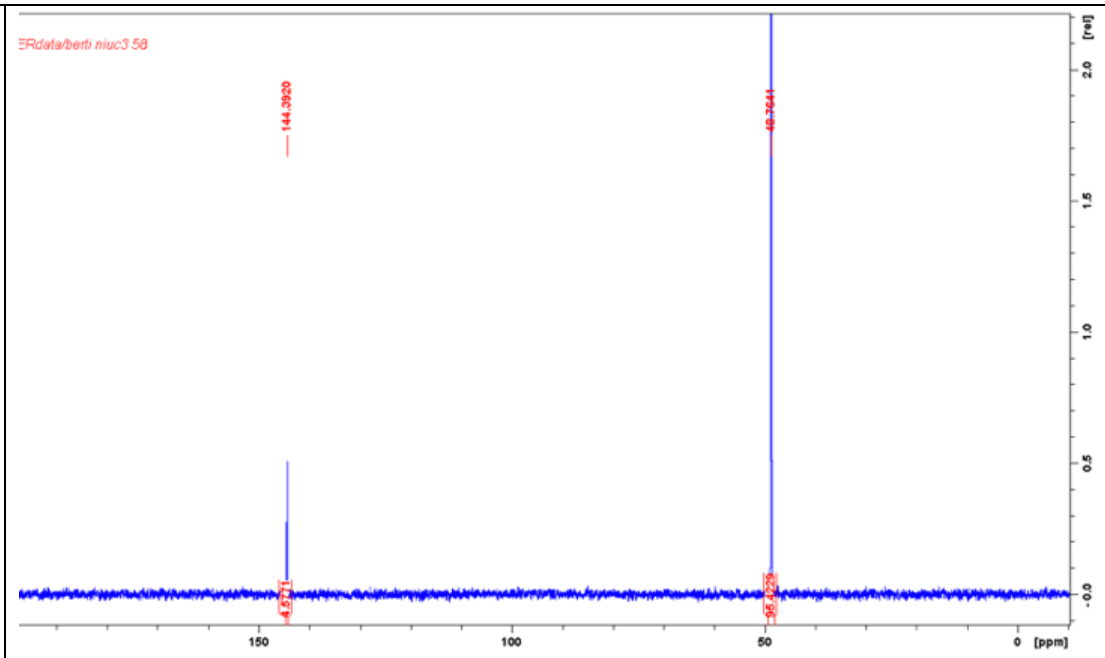

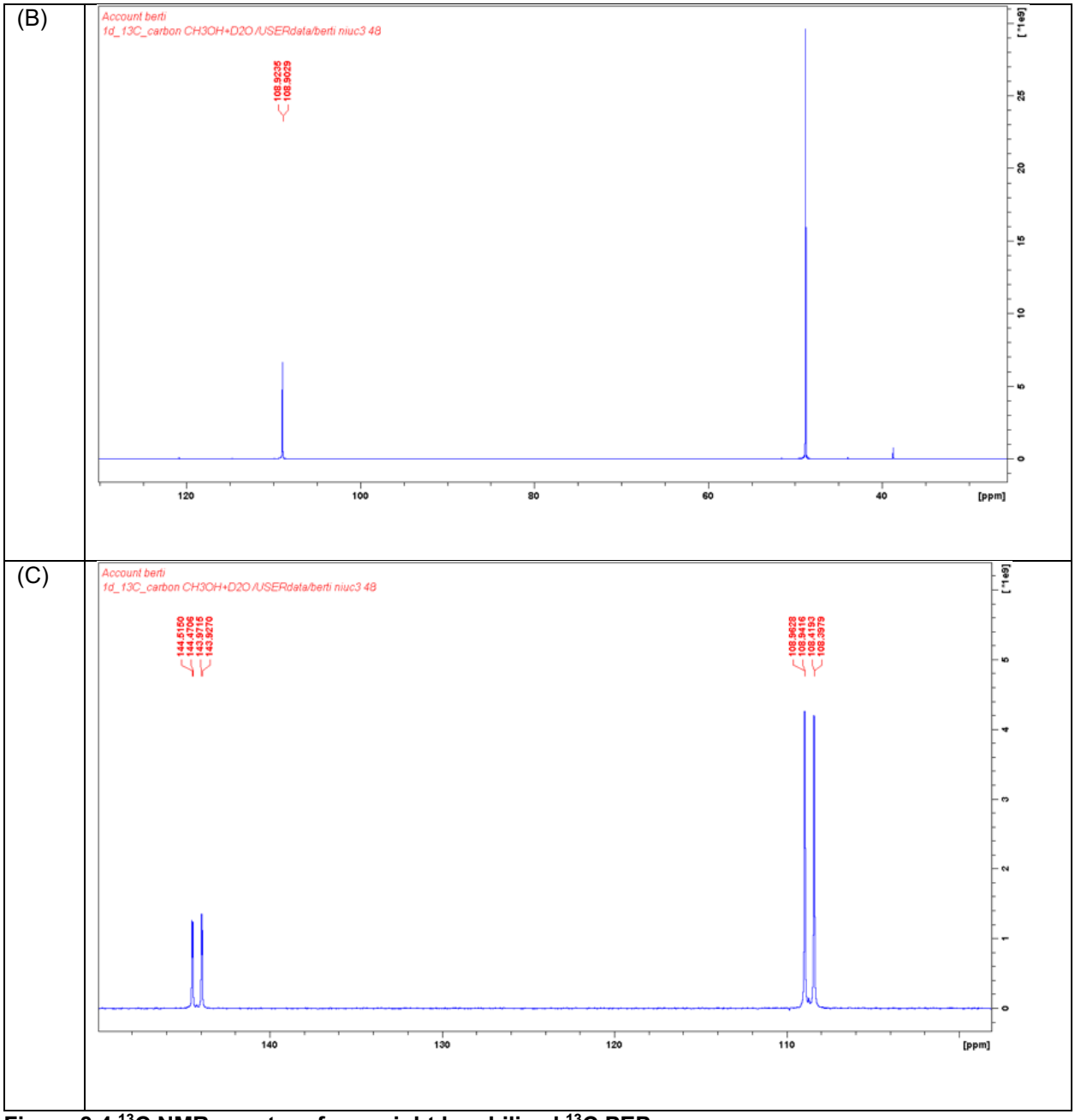

Figure 3.4 ^{13}C NMR spectra of overnight lyophilized ^{13}C PEP.

A: [2-^{13}C] PEP; B: [3-^{13}C] PEP; C: [2,3-^{13}C] PEP.

Table 3.1 ^{13}C NMR chemical shift of ^{13}C PEP.

Product	Peak 1		Peak 2	
	Chemical shift (ppm)	Coupling	Chemical shift (ppm)	Coupling
A: [2-^{13}C] PEP	NA	NA	144.39	s

B: [3-^{13}C] PEP	108.9	d, $^{1}J_{C-P}$ = 12.8 Hz	NA	NA
C: [2,3-^{13}C] PEP	108.3-108.9	q, $^{1}J_{C3-P}$ = 3.2 Hz, $^{1}J_{C2-C3}$ = 82 Hz	143.9-144.5	q, $^{1}J_{C2-P}$ = 6.7 Hz, $^{1}J_{C2-C3}$ = 82.2 Hz

3.3.3 ^{18}O-PEP

For the measurement of the [2-^{18}O]PEP KIE, the bridging oxygen of PEP must be labelled with ^{18}O. The keto oxygen of pyruvate quickly exchanges with ^{18}O when dissolved in $H_2{}^{18}O$-containing buffer. Running the ppsA synthesis reaction as usual then yielded [2-^{18}O]PEP, which was purified as described above. Its identity was verified by ^{31}P-NMR (Figure 3.5).

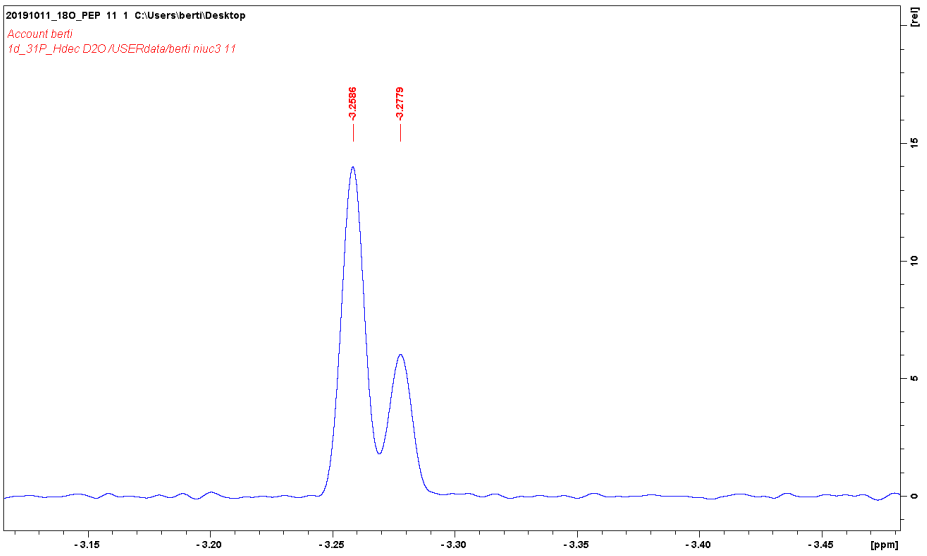

Figure 3.5 ^{31}P-NMR spectra of [2-^{18}O]PEP.

Chemical shift: [2-^{16}O]PEP: -3.26 ppm; [2-^{18}O]PEP: -3.28 ppm. NMR data was processed with parameter gb = 0.1, and lb = -2.8.

After lyophilization, 1.2 mL [2-^{18}O]PEP was recovered. The concentration of [2-^{18}O]PEP was measured by PK/LDH coupled assay adding 5 µL of reaction mix to a total volume of 1 mL assay reaction mix (Figure 3.6). The total yield was about 60%.

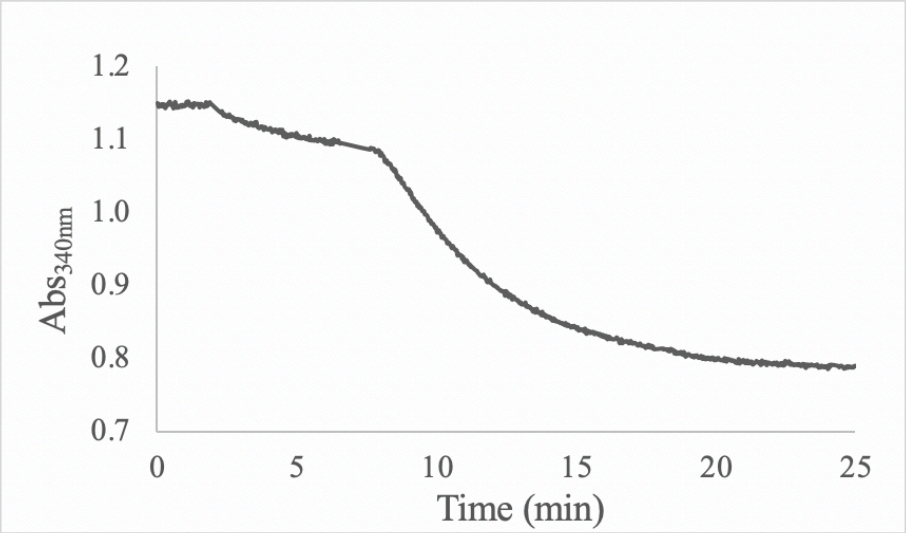

Figure 3.6 Coupled PK/LDH assay to determine [2-^{18}O]PEP concentration.

Table 3.2 Coupled PK/LDH assay to determine [2-^{18}O]PEP concentration.

Enzyme	Start A_{340}	End A_{340}	ΔA_{340}	Dilution factor	Concentration (mM)
LDH (sodium pyruvate → lactate)	1.149	1.094	0.055	200	1.77
PK (PEP → sodium pyruvate → lactate)	1.094	0.786	0.308	200	9.90

3.3.4 E4P

E4P was synthesized from G6P and lead acetate (Figure 3.7). The reaction mix was loaded onto a 5 mL Q-Sepharose column and E4P was eluted from 12 to 24 min. The contents of the eluted fractions were confirmed with the reducing sugar assay to detect E4P and G6P, the G6P dehydrogenase assay to detect G6P and the DAHPS enzymatic assay to detect E4P. E4P-containing fractions were then eluted with ddH_2O on SP-Sepharose column to remove ammonium ions. Purified E4P was verified by both ^{1}H-NMR and ^{31}P-NMR (Figure 3.8). The concentration was determined by DAHPS enzymatic assay with varying volumes of E4P product

and excess PEP to drive the reaction to completion. The result was (3.7 ± 0.4) mM, and the total yield was 30%.

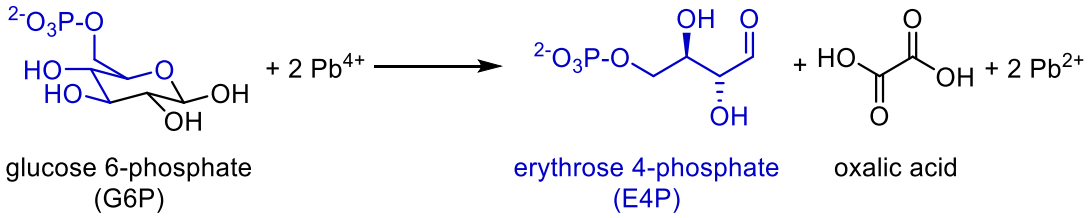

Figure 3.7 E4P synthesis reaction.

The E4P synthesis reaction was based on references[25,140].

(A)

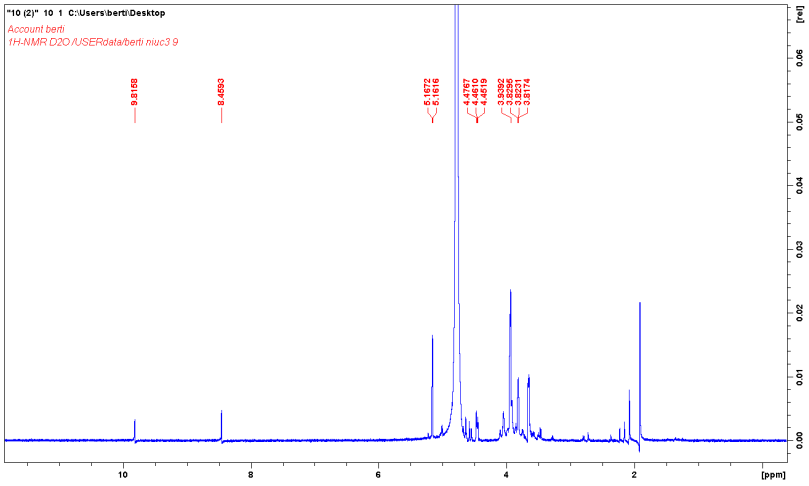

(B)

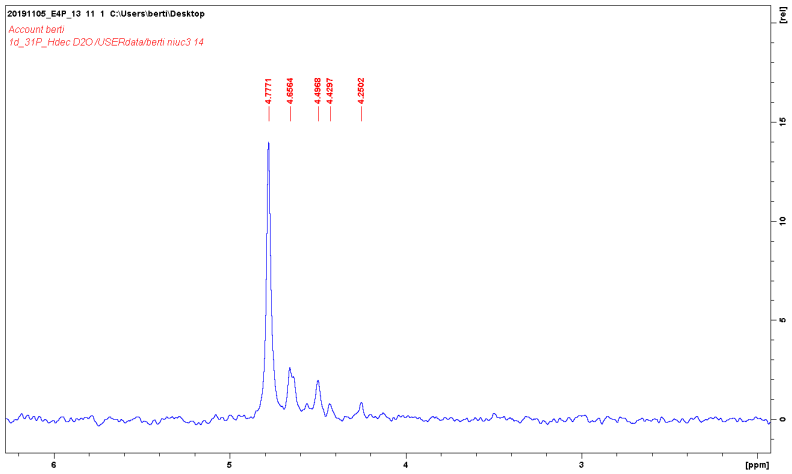

Figure 3.8 NMR spectra of E4P

(A)^{1}H-NMR spectrum, (B) ^{31}P-NMR spectrum.

Table 3.3 Assignment of ^{1}H-NMR and ^{31}P-NMR peaks.

Product	Nucleus	Chemical shift (ppm)	Assignment
E4P	^{1}H	9.82	E4P aldehyde
		8.46	formate
		3.81-5.18	Other E4P protons
	^{31}P	4.25-4.78	NA

3.4 Reaction conditions for KIE measurements

3.4.1 Cd^{2+} as an essential activator of DAHPS

The goal is to measure isotope ratios (and therefore KIEs) on live reactions as they run in the NMR tube. DAHPS is divalent metal ion dependent, and the metal normally used in rate assays, Mn^{2+}, is paramagnetic, which cannot be observed by high-resolution NMR. Paramagnetic ions decrease relaxation times and thus increase peak widths. Therefore, a diamagnetic divalent metal ion, Cd^{2+}, was investigated for its ability to activate DAHPS. It does activate the enzyme, but there is an abrupt drop in rates above 20 μM Cd^{2+} (Figure 3.9). The cause of this drop is not known. Nonetheless, it should be possible to run reactions in the NMR tube as long as Cd^{2+} $\leq$ 20 μM.

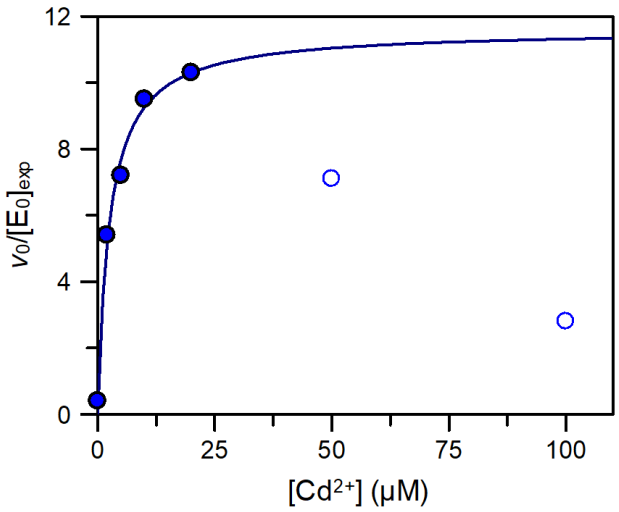

Figure 3.9 Enzymatic DAHPS assay.

Values of $v_0/[E_0]$ under varying Cd^{2+} concentration for both 1mM PEP and 2mM PEP are shown. In both groups, the highest value of $v_0/[E_0]$ were found at 20 μM Cd^{2+}.

3.5 NMR acquisition

The relationship between relaxation times and accurate quantification is complex. There are two relaxation modes, longitudinal, T_1, and transverse, T_2. It is always the case that $T_1 \geq T_2$, [115], though in this study, $T_1 >> T_2$. Accurate quantification requires complete longitudinal relaxation, with relaxation times of $7 \times T_1$. For ^{31}P PEP and P_i and ^{13}C in pyruvate (and presumably PEP), $T_1 \sim 15$ s, so $7 \times T_1 \sim 2$ min, which would lead to very long data collection times. If it were possible to decrease T_1 using a paramagnetic relaxation agent without affecting T_2 (or T_2*), it would be possible to use shorter delay times. However, very short T_2* times causes peak broadening, so it would be necessary to decrease T_1 while not decreasing T_2* to the point that resolution between the ^{16}O-^{31}P and ^{18}O-^{31}P peaks is lost.

3.5.1 T_1 measurement conditions

Several factors shorten T_1 relaxation times, including oxygen. O_2 is a paramagnetic gas[144]. The unpaired spins on oxygen can cause the relaxation by dipolar interaction. Paramagnetic metal ions, like Gd^{3+} and Mn^{2+}, can also speed up the relaxation process. These effects can be reduced by chelating paramagnetic metal ions using Chelex 100 and removing dissolved oxygen by degassing the sample. NMR samples were routinely demetallated and degassed in order to reproducibly obtain intrinsic T_1 values.

3.5.2 T_1 measurement with relaxation agent

Gadolinium chloride ($GdCl_3$) is a commonly used relaxation agent. Varying concentration of Gd^{3+} was added to degassed [1-^{13}C]pyruvate solution. T_1s were measured on each sample on a 200 MHz NMR (Figure 3.10).

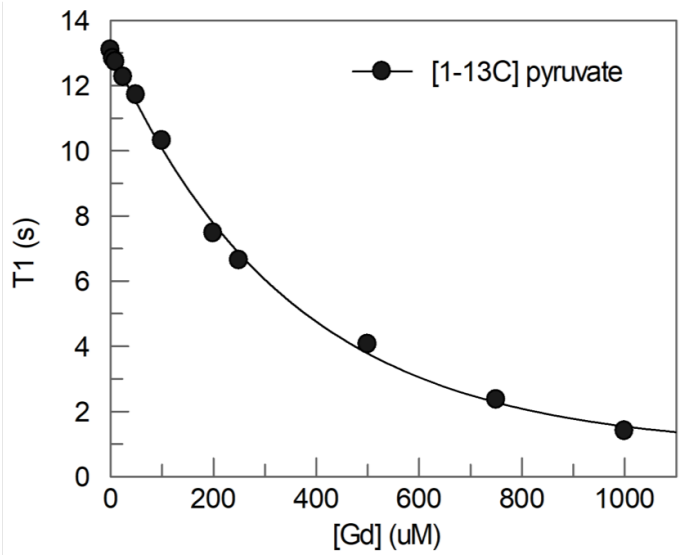

Figure 3.10 T_1 measurement of [1-^{13}C] pyruvate at 200 MHz.

Table 3.4 Effect of Gd^{3+} on T_1 of [1-^{13}C] pyruvate.

Parameter for [1-^{13}C] pyruvate	Value (± standard error)
T_1 (no Gd^{3+})	13.1 (± 0.1) s
[Gd^{3+}] dependence	350 (± 20)
$T_{1, inf}$	0.8 (± 0.3) s

[a] Fitted to (Eq. **1.9**).

Out of concern that free Gd^{3+} might disrupt DAHPS activity, the effect on T_1 of Gd^{3+} binding to deferoxamine B (DFO), a chelator, was investigated. The DFO concentration was at least 10 times Gd^{3+} to ensure that no free Gd^{3+} existed. Similar results was found in T_1 of ^{13}C (Figure 3.11A), but not in T_1 of ^{31}P (Figure 3.11B). T_1 initially decreased with increasing [Gd^{3+}], but then increased when [Gd^{3+}·DFO] was > 50 μM. For that reason, the T1 values were not fitted to (Eq. **1.9**).

(A)

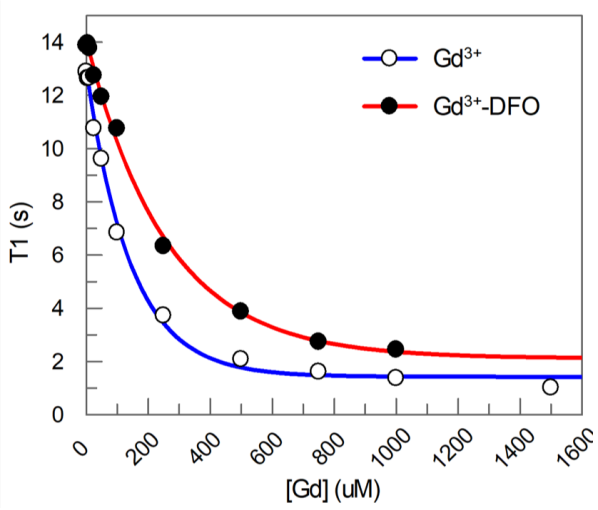

(B)

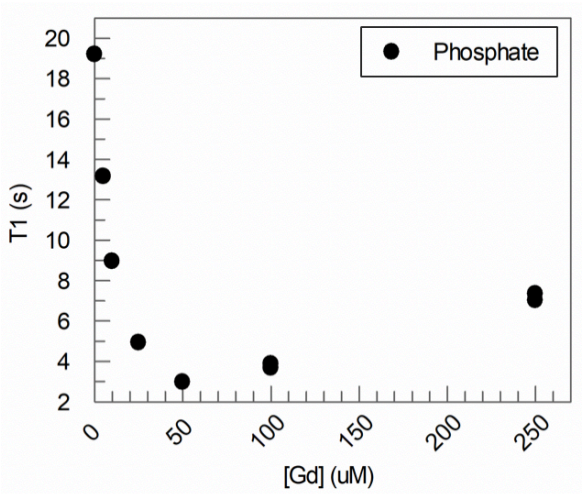

Figure 3.11 Effects of Gd^{3+} on T_1.

T_1 was measured for at varying concentrations of Gd^{3+} for (A) [1–^{13}C]pyruvate in the presence and absence of the chelator DFO, and (B) P_i in the presence of DFO, at 200 MHz.

Table 3.5 T_1 parameters for [1-^{13}C]pyruvate with Gd^{3+} and Gd^{3+}-DFO.

T_1 parameter of ^{13}C [a]	Value (± standard error)	
	Gd^{3+}	Gd^{3+}-DFO
T_1 (no Gd^{3+})	13.0 (± 0.2) s	14.1 (± 0.1) s
[Gd^{3+}] dependence	143 (± 10)	258 (± 18)
$T_{1,\,inf}$	1.4 (± 0.2) s	2.1 (± 0.3) s

[a] Fitted to (Eq. **1.9**).

3.5.3 T_1 measurement at different field strengths

For T_1 relaxation to occur, there must be a magnetic field fluctuating at the Larmor precession frequency (ν_0), which is directly proportional to the field strength (B_0) of the spectrometer. So, the T_1 relaxation time is dependent on the field strength. Their relationship was investigated by measuring the ^{13}C T_1 on 200 MHz and 600 MHz (Figure 3.12). This suggests that T_1 increases modestly as the field strength becomes higher, but not enough to significantly affect KIE measurements.

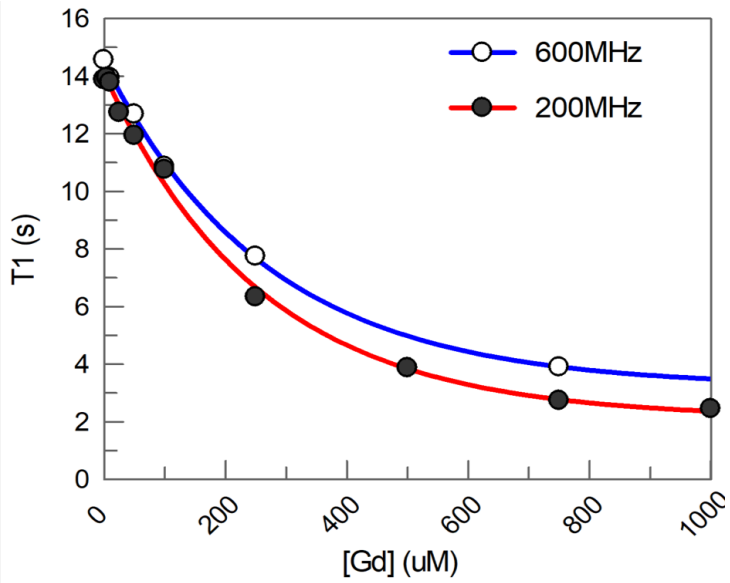

Figure 3.12 T_1 as a function of field strength.

T_1 values for [1-^{13}C]pyruvate in the presence of Gd^{3+} were measured on the 200 MHz and 600 MHz spectrometers.

Table 3.6 T_1 parameters for [1-^{13}C pyruvate under different field strengths.

T_1 parameters of ^{13}C [a]	Value (± standard error)	
	200 MHz	600 MHz
T_1 (no Gd^{3+})	14.1 (± 0.1) s	14.5 (± 0.1) s
[Gd^{3+}] dependence	258 (± 18)	270 (± 13)
$T_{1, inf}$	2.1 (± 0.2) s	3.2 (± 0.2) s

[a] Fitted to (Eq. **1.9**).

3.5.4 Line broadening effect of Gd^{3+}

Using Gd^{3+} as a relaxation agent could be a solution to reduce measurement time and be used in KIEs measurement. However, it reduces T_2* (Figure 3.13) and increases peak width (Figure 3.14), leading to the loss of resolution and potential missing peak splittings.

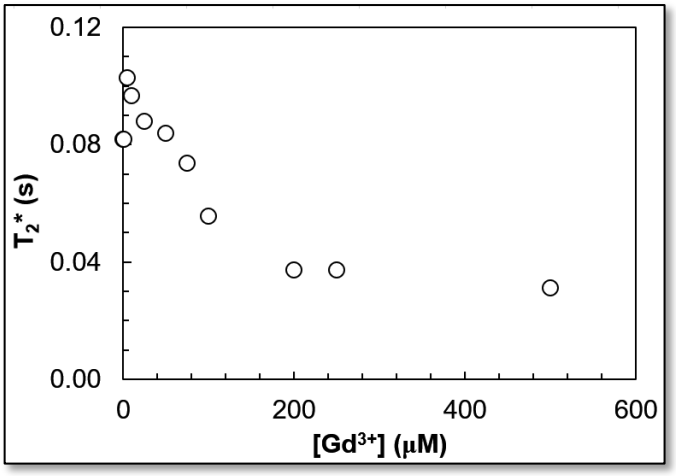

Figure 3.13 Gd^{3+} decreases T_2*.

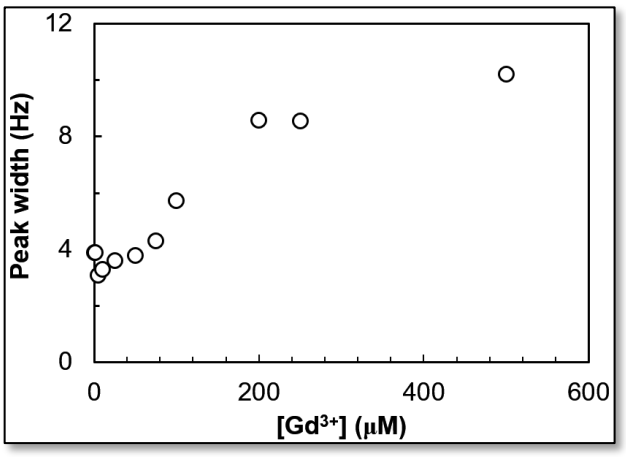

Figure 3.14 Gd^{3+} increases peak width.

As a result, Gd^{3+} is not ideal for measurement of isotope ratios. To reduce measurement time, a new pulse program with shorter repetition time was investigated.

3.6 NMR processing

The FIDs acquired during NMR data collection can be adjusted before applying Fourier transformation (FT) to increase S/N or improve the spectral resolution, though improving one parameter necessarily worsens the other. This method is known as windows functions. The signal intensity of an FID declines with time, while noise remains constant throughout the acquisition time, meaning that the noise level is relatively greater in the latter part of the FID. The noise can be diminished by de-emphasizing the latter part of FID by applying an exponential multiplication (em) function. However, while applying a strong em function will improve the S/N, it will be at the expense of line broadening, causing a reduction of peak heights and peak separation. The extent of line broadening is determined by the decay rate of the FID signal, and is defined directly by line broadening (lb) parameter in Bruker's Topspin software. Values of lb = 0.3 - 1.0 Hz are typical, while values > 10 Hz may be applied to noisy spectra. Low lb values enhance the signal sensitivity and minimize line broadening.

Integration is typically performed in NMR software by defining an integral region around the resonances of interest, then summing the intensity at each point in the spectrum to calculate the peak area. Peak shapes do not affect the result of integration, but the peaks must be baseline separated and the integration region should extend at least 20 times the line width in both directions. Achieving an accuracy of 0.1%, the regions would have to cover 75 times the peak width in both directions.

This extent of peak separation is not possible for measuring isotope ratios (see, for example, Figure 3.15), so an alternate approach, peak deconvolution, must be used. Voigt deconvolution, which includes a mix of Lorentzian (the "natural" NMR peak shape) and Gaussian (instrument caused) peak shape functions is commonly used to fit peaks, especially for those asymmetrical peaks caused by poor shimming[145].

Initially, TopSpin was used to fit a Lorentzian-Gaussian peak shape to overlapped resonances. However, the lack of adjustable fitting parameters and the observed variability in deconvolution results make it less trustworthy. Another program, PeakFit, was used to deconvolute overlapping peaks. Two different models, Lorentzian deconvolution (Figure 3.15A), and Voigt deconvolution (Figure 3.15B), which is a combination of Lorentzian and Gaussian deconvolution have been applied. Since Voigt deconvolution take into account that both contributions from the natural Lorentzian peak shape and from the instrument, it achieves a better result.

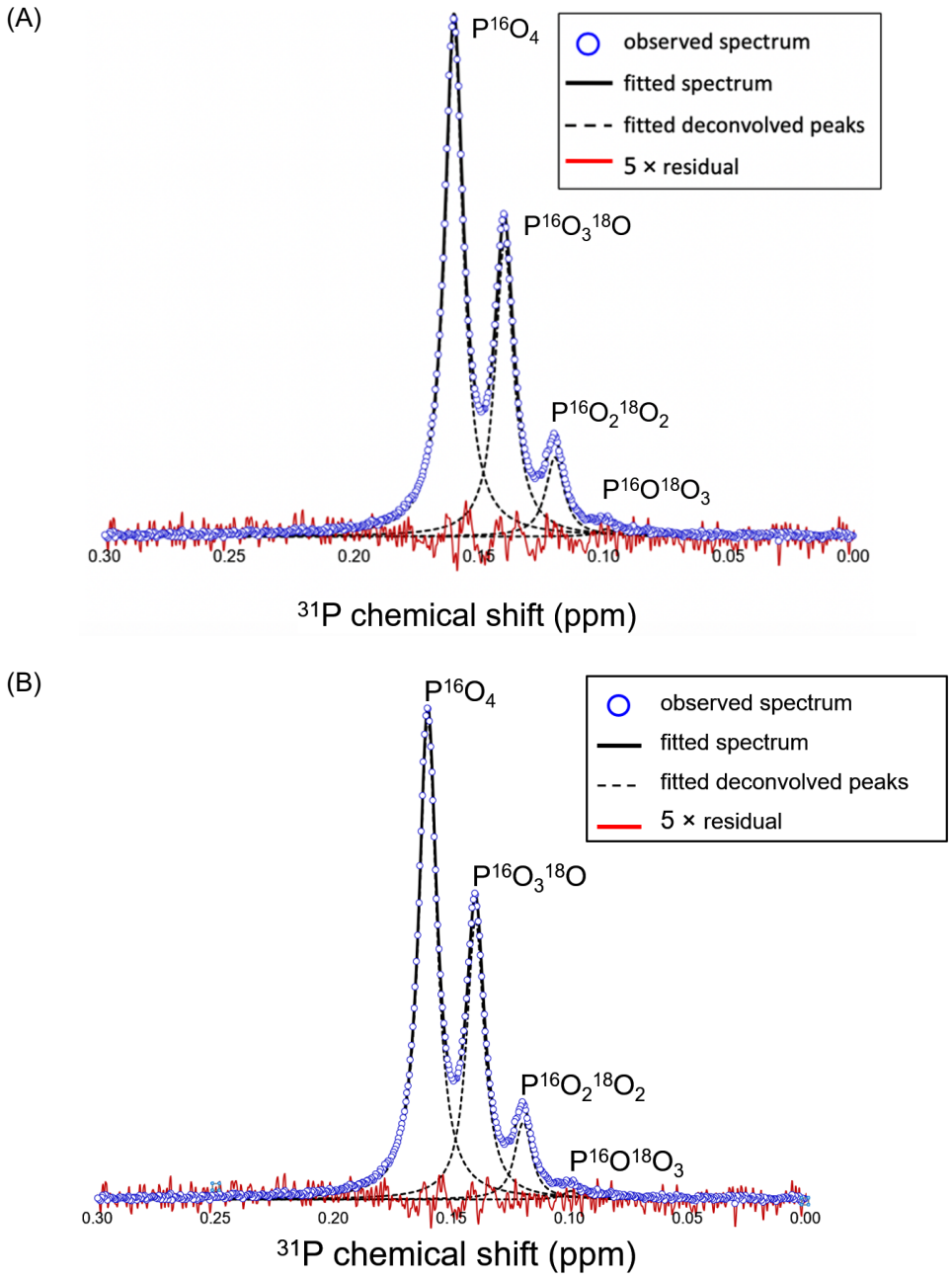

Figure 3.15 NMR peak deconvolution.

Two different fitting models were used to deconvolve a ^{31}P spectrum of ^{18}O-labelled Pi. (A) Lorentzian deconvolution, and (B) Voigt deconvolution. The experimental spectra (○) are shown, along with the deconvolved spectra (solid line) and individual deconvolved peaks (dashed lines). The residual at each point in the experimental spectrum ($I_{obs} - I_{fitted}$) is multiplied by 5 to make the residual visible. ^{18}O-labelled P_i was produced by acid-catalyzed exchange of phosphoric acid in $H_2{}^{18}O$.

3.7 Standard curves of isotope ratios

3.7.1 ^{18}O-labeled phosphoric acid

For preliminary spectra, ^{18}O-labeled P_i was used for ^{31}P NMR as it is more accessible than [2-^{18}O]PEP and has similar T_1 values. [$^{18}O_n$]Pi was made using acid-catalyzed exchange of $H_2{}^{18}O$ into phosphoric acid. ^{18}O-labeled phosphoric acid was confirmed by ^{31}P-NMR (Figure 3.16).

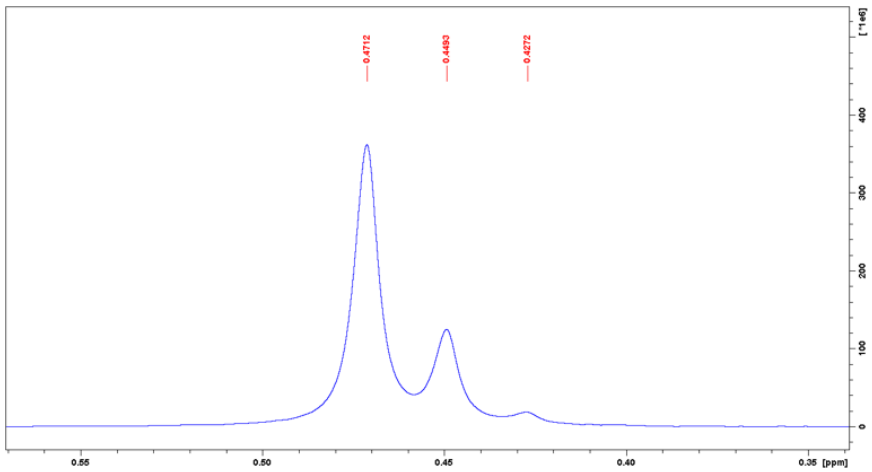

Figure 3.16 ^{31}P NMR spectrum of ^{18}O exchanged phosphoric acid.

Chemical shift: $P^{16}O_4$: δ, 0.4712 ppm; $P^{16}O_3{}^{18}O_1$: δ, 0.4493 ppm; $P^{16}O_2{}^{18}O_2$: δ, 0.4272 ppm.

3.7.2 Standard curves of ^{16}O/^{18}O

PeakFit was used to fit the standard curve of the ratio of ^{16}O/^{18}O obtaining from two different pulse programs. The ^{16}O/^{18}O ratio was measured in ^{18}O-labelled P_i, then measured again after standard additions of unlabelled P_i to change the ration. The conventional pulse program used a 90° flip angle, followed by a $7 \times T_1 = 119$ s relaxation time before the next pulse. It took 6 h to measure to the isotope ratio of each point on the standard curve. The incomplete relaxation pulse program used a 30° flip, approximately the Ernst angle and a repetition time of

$0.2 \times T_1 = 3.5$ s. The repetition time was selected based on the T_2* value such that the pulse was repeated as soon as the FID had decayed to zero. In this way, "dead time"; i.e., the time between the end of a measurable FID and the next pulse, was minimized. This shortened the time for measurement of isotope ratio for each point to only 40 min.

The standard curve constructed using a 'new pulse program' achieved a similar standard error in the slope, $\pm$ 0.021, compared to that of the conventional pulse program, $\pm$ 0.022, making it a 9-fold faster method to measure isotope ratios (Figure 3.17). The pulse programs gave slightly different slopes in the standard curves, namely 1.126 ± 0.022 for $7 \times T_1$ versus slope = 1.073 ± 0.021 for $0.2 \times T_1$. The difference in slopes is not significant; propagating the differences into an experimental KIE would lead to a 0.05% error, i.e., a KIE of 1.0100 would become 1.0105, not a significant difference.

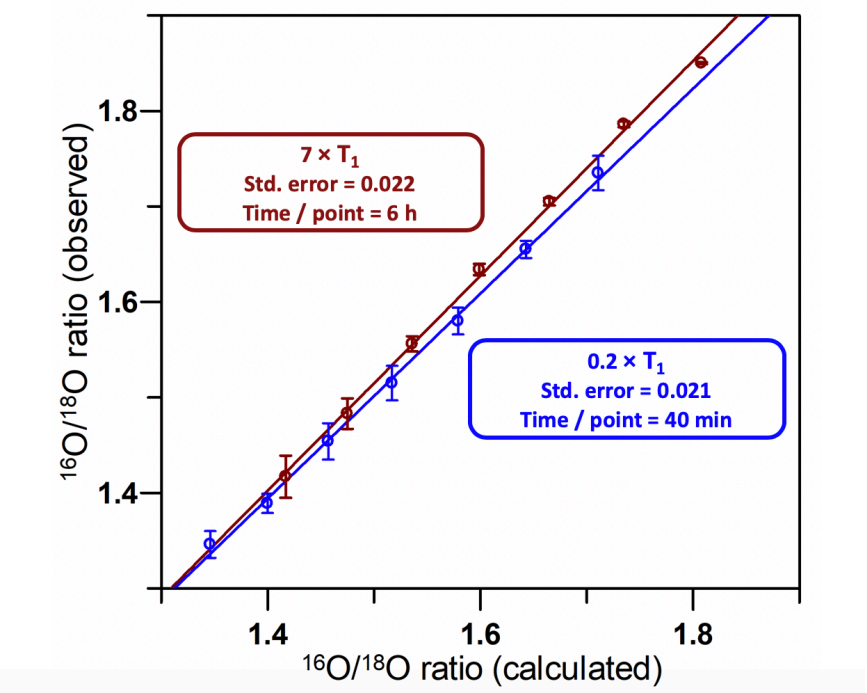

Figure 3.17 Effect of delay time on $^{16}O/^{18}O$ isotope ratio measurement.

Standard curves of $^{16}O/^{18}O$ fitted by PeakFit to a conventional and incomplete relaxation pulse program. Aliquots of $P^{16}O_4$ were added to ^{18}O-labelled P_i and spectra were collected using delay times of 7 × or 0.2 × T1. (red) 7 × T1 (119 s), 90° pulses, slope = 1.126 ± 0.022. (blue) 0.2 × T1 (3.5 s), 30° pulses, slope = 1.073 ± 0.021.

4 Discussion

4.1 PEP synthesis

The method for synthesizing ^{13}C-PEP was developed previously that used anion exchange for PEP purification. This method left high salt concentrations in the product, which decreases NMR sensitivity and increases sample heating. In this work, an ion-paired reverse phase purification method was developed which, when coupled with a cation exchange column to remove the residual salt ($DIEA^+$) achieved a 'clean' preparation. The strong cation exchange resin has sulfopropyl groups and can be charged with H^+. $DIEA^+$ ion can be replaced by H^+ while the PEP running though the column.

Additionally, an enzymatic synthesis method was developed in this work. [2-^{18}O]PEP was synthesized in ppsA-catalyzed reaction in 50% ^{18}O water. Previously, ^{18}O-PEP synthesized using traditional organic synthesis[33]. The traditional method was more difficult, and could not readily be adapted to incorporating multiple isotopic labels. Our original plan was to measure the ^{18}O KIEs using [^{13}C,^{18}O] labelled PEPs, so it was important to be able to make [3-^{13}C, 2-^{18}O]PEP, which can be synthesized with enzymatic synthesis method using [3-^{13}C]PEP as substrate. The enzymatic synthesis method demonstrates that ^{18}O was incorporated by ppsA, and that the incorporation level was roughly equal to the ^{18}O content of the solvent.

4.2 E4P synthesis

E4P was synthesized by oxidative degradation of G6P and purification by anion exchange. The initial protocol was to react G6P completely with excess lead tetraacetate. However, the excess Pb^{4+} was able to further oxidize E4P to glyceraldehyde 3-phosphate. So, the method was modified to use 1.7 equivalents of lead tetraacetate, 85% of the stoichiometric

amount[140]. Pb^{4+} consumption was monitored using starch-iodide indicator paper. At the point where not all the added Pb^{4+} was consumed, an additional 5% of G6P was added to exhaust the excess Pb^{4+}, and the reaction was stopped.

During the purification, a large amount of P_i co-eluted with E4P, as detected with the MG/AM colorimetric assay. The source was eventually determined to be breakdown of E4P and/or residual G6P while water was being removed with heating on the rotary evaporator. Switching to a high vacuum source without heating reduced the temperature to ≈ −5 °C during solvent removal, which greatly reduced the amount of contaminating P_i in E4P. In addition, any P_i-containing fractions during E4P purification were not pooled.

Purified E4P was quantified in DAHPS enzymatic assay with excessive PEP and varying amount of E4P. The overall yield was low, which possibly because E4P tends to form a dimer when it is too concentrated (Figure 4.1)[146], while in DAHPS assay, E4P is a monomer. Since the dimerization is reversible, E4P was diluted and quantified with the same condition. The overall yield was improved to 30%.

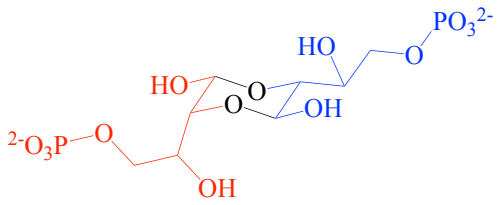

Figure 4.1 E4P dimer.

E4P dimer was characterized previously by NMR[146].

4.3 NMR methods

4.3.1 Relaxation agent

The relaxation agent $GdCl_3$ was able to significantly shorten T_1 relaxation times and speed up the measurement process. However, it also reduced the effective T_2 relaxation time, T_2*. Peak width at half height ($\nu_{\frac{1}{2}}$) is solely determined by T_2* by the equation:

$$\nu_{\frac{1}{2}} = \frac{1}{\pi \cdot T_2^*}$$

The decrease of T_2* will reduce the peak width at half height, leading to line-broadening, which would interfere with the measurement of isotope ratios. Consequently, paramagnetic relaxation agent is not useful in KIEs measurements, in spite of its great effect on decreasing the measurement time.

4.3.2 Acquisition time

Acquisition time is an important parameter in NMR measurement. It has to be long enough to capture the entire FID signal without truncation (Figure 1.14). Later times in the FID are important as they define the peak resolution. However, collecting the FID after the signal is no longer visible will increase noise without increasing the signal.

4.3.3 Short repetition time and optimal flip angle

Using 90° flip angle and $7 \times T_1$ as repetition time generates maximum signal and enhances S/N. However, during the acquisition, most of the time is wasted on in the delay time while waiting for longitudinal relaxation to be complete. Since relaxation agents proved not to be

effective for accelerating relaxation, another method to accelerate isotope ratio measurements had to be found. In this case, using shorter repetition time between pulses and optimal flip angle can of help to achieve efficient measurement. Shorter repetition time decreases the signal after the first FID, however, this can be compensated by using increased number of scans in a given period of time. With an optimal flip angle less than 90°, the z component of magnetization is reduced, so the time required for its relaxation is less. The relationship between repetition time and flip angel is determined by (Eq. **1.8**). It has been found that this method gives a gain in S/N that can be as large as 1.58, and is always better than 90° flip angle with longer waiting time[122].

This method is dependent on the accurate measurement of T_1 of nucleus of interest. So, the great effort should be taken in both sample preparation and T_1 measurement. For sample preparation, the metal ion should be removed by chelator, and the oxygen should be removed by degassing as they both interfere with the T_1 measurement. During T_1 measurement, a list of delay time is created. Among these numbers, at least one delay time should be $7 \times T_1$ representing full relaxation. And the peak should be correctly phased as the peak area is essential for determining T_1.

4.3.4 Deconvolution method

The result of using Voigt deconvolution for peak fitting confirms that it is a better fitting model for deconvolution. It generates smaller residual between observed data and fitting curve, especially at regions where peaks are overlapped, which are essential for determining peak areas of each individual peaks. The Peakfit software also enables us to adjust Lorentzian/Gaussian composition of NMR peaks to achieve the best fitting result, while this cannot be done using TopSpin built-in deconvolution application.

To summarize, this work has determined both NMR acquisition and processing parameters to achieve enhanced S/N, as well as to shorten the measurement time.

5 Concluding Remarks

5.1 Conclusions

In this work, methods of synthesizing and purifying labeled substrates ^{13}C-PEP, ^{18}O-PEP, unlabeled substrate E4P have been characterised. A pulse program which utilizes 'Ernst angle' as flip angle has been used in substitution of the conventional pulse program with full relaxation of magnetization to measure isotope ratio. It has been validated that this new pulse program achieves similar standard error in constructed standard curve of ^{16}O/^{18}O and decreases measurement time 9-fold. Post-acquisition data process is also evaluated. Voigt deconvolution method has been employed to determine peak areas in overlapped peaks to achieve accurate results compared to Lorentzian deconvolution model.

5.2 Future directions

With all the preliminary work finished, KIEs at different positions can be measured using qNMR while the reaction going in the NMR tube. To calculate KIEs, both isotopologues ratio and conversion of reaction should be measured. For isotopologues ratio, it can be calculated from the ratio of corresponding peak ratios. For conversion of reaction, it can be measured using an external reference in a coaxial NMR insert tube. For example, for ^{31}P measurement, the external reference could be phosphoric acid or monomethyl phosphate. With known concentration and known volume of coaxial insert, it generates a standard peak next to the substrates and product peaks. By comparing the substrates and product peaks against standard peak, the conversion of reaction can be calculated. With several groups of data of isotopologues ratios and conversions of reaction, experimental KIEs can be calculated by fitting with the equation mentioned above.

Computational chemistry is then used to interpret the experimental KIEs. A match between calculated KIEs of computational TS structures and calculated KIEs suggests that computational TS structure could be the actual TS structure. As a result, a specific mechanism or a mixed mechanism in DAHPS reaction can be verified.

6 References

(1) Gould, I. M.; Bal, A. M. New Antibiotic Agents in the Pipeline and How Hey Can Help Overcome Microbial Resistance. *Virulence* **2013**, *4*, 185–191.

(2) Ventola, C. L. The antibiotic resistance crisis: part 1: causes and threats. *J. Clin. Pharm. Ther.* **2015**, *40*, 277.

(3) Sengupta, S., Chattopadhyay, M. K., & Grossart, H. P. The multifaceted roles of antibiotics and antibiotic resistance in nature. *Front. Microbiol.* **2013**, *4*, 47.

(4) Davies, J., & Davies, D. Origins and evolution of antibiotic resistance. *Microbiol. Mol. Biol. Rev.* **2010**, *74*, 417-433.

(5) Fleming, A. On the antibacterial action of cultures of a penicillium, with special reference to their use in the isolation of B. influenzae. *Brit. J. Exp. Path.* **1929**. *10*, 226.

(6) Abraham, E. P.; Chain, E. An Enzyme from Bacteria Able to Destroy Penicillin. 1940. *Rev. Infect. Dis.* **1988**, *10*, 677–678.

(7) Spellberg, B.; Gilbert, D. N. The Future of Antibiotics and Resistance: A Tribute to a Career of Leadership by John Bartlett. *Clin. Infect. Dis.* **2014**, *59*, S71–S75.

(8) Read, A. F.; Woods, R. J. Antibiotic Resistance Management. *Evol. Med. Public Heal.* **2014**, *2014,* 147.

(9) Lushniak, B. D. Antibiotic Resistance: A Public Health Crisis. *Public Health Rep.* **2014**, *129*, 314–316.

(10) Viswanathan, V. K. Off-Label Abuse of Antibiotics by Bacteria. *Gut Microbes* **2014**, *5*, 3-4.

(11) Luyt, C. E.; Bréchot, N.; Trouillet, J. L.; Chastre, J. Antibiotic Stewardship in the Intensive Care Unit. *Crit. Care.* **2014**, *18*, 480.

(12) Munita, J. M.; Arias, C. A. Mechanisms of antibiotic resistance. *Microbiol. Spectr.* **2016**, *4*, 481-511.

(13) Wright, G. D. Antibiotics: a new hope. *Chem. Biol.* **2012**, *19*, 3-10.

(14) Aminov, R. I. A brief history of the antibiotic era: lessons learned and challenges for the future. *Front. Microbiol.* **2010**, *1*, 134.

(15) Bentley, R.; Haslam, E. The Shikimate Pathway-A Metabolic Tree with Many Branche. *Crit. Rev. Biochem. Mol. Biol.* **1990**, *25*, 307–384.

(16) Bravo, I. G., García-Vallvé, S., Romeu, A., Reglero, Á. Prokaryotic Origin of Cytidylyltransferases and α-Ketoacid Synthases. *Trends Microbiol.* **2004**, *12*, 120–128.

(17) Pratap, S., Dev, A., Kumar, V., Yadav, R., Narwal, M., Tomar, S., & Kumar, P. Structure of chorismate mutase-like domain of DAHPS from Bacillus subtilis complexed with novel inhibitor reveals conformational plasticity of active site. *Sci. Rep.* **2017**, *7*, 1-15.

(18) Cross, P. J.; Dobson, R. C. J.; Patchett, M. L.; Parker, E. J. Tyrosine Latching of a Regulatory Gate Affords Allosteric Control of Aromatic Amino Acid Biosynthesis. *J. Biol. Chem.* **2011**, *286*, 10216–10224.

(19) Cross, P. J.; Pietersma, A. L.; Allison, T. M.; Wilson-Coutts, S. M.; Cochrane, F. C.; Parker, E. J. Neisseria Meningitidis Expresses a Single 3-Deoxy-D-Arabino-Heptulosonate 7-Phosphate Synthase That Is Inhibited Primarily by Phenylalanine. *Protein Sci.* **2013**, *22*, 1087–1099.

(20) Webby, C. J.; Jiao, W.; Hutton, R. D.; Blackmore, N. J.; Baker, H. M.; Baker, E. N.; Jameson, G. B.; Parker, E. J. Synergistic Allostery, a Sophisticated Regulatory Network for the Control of Aromatic Amino Acid Biosynthesis in Mycobacterium Tuberculosis. *J. Biol. Chem.* **2010**, *285*, 30567–30576.

(21) Ducati, R.; Basso, L.; Santos, D. Mycobacterial Shikimate Pathway Enzymes as Targets for Drug Design. *Curr. Drug Targets* **2007**, *8*, 423–435.

(22) Maeda, H.; Dudareva, N. The Shikimate Pathway and Aromatic Amino Acid Biosynthesis in Plants. *Annu. Rev. Plant Biol.* **2012**, *63*, 73–105.

(23) Tohge, T., Watanabe, M., Hoefgen, R., & Fernie, A. R. Shikimate and phenylalanine biosynthesis in the green lineage. *Front. Plant Sci.* **2013**, *4*, 62.

(24) Srinivasan, P. R., & Sprinson, D. B. 2-Keto-3-deoxy-D-arabo-heptonic acid 7-phosphate synthetase. *J. Biol. Chem.* **1959**, *234*, 716-722.

(25) Balachandran, N. DAHP Oxime: A Transition State Mimic Inhibitor Of DAHP Synthase Doctoral Dissertation, McMaster University, Canada, **2014**.

(26) M. Dewick, P. The Biosynthesis of Shikimate Metabolites. *Nat. Prod. Rep.* **1998**, *15*, 17.

(27) Grison, C.; Petek, S.; Finance, C.; Coutrot, P. Synthesis and Antibacterial Activity of Mechanism-Based Inhibitors of KDO8P Synthase and DAH7P Synthase. *Carbohydr. Res.* **2005**, *340*, 529–537.

(28) Light, S. H., & Anderson, W. F. The diversity of allosteric controls at the gateway to aromatic amino acid biosynthesis. *Protein Sci.* **2013**, *22*, 395-404.

(29) McArthur, J. D.; West, N. P.; Cole, J. N.; Jungnitz, H.; Guzmán, C. A.; Chin, J.; Lehrbach, P. R.; Djordjevic, S. P.; Walker, M. J. An Aromatic Amino Acid Auxotrophic Mutant of

Bordetella Bronchiseptica Is Attenuated and Immunogenic in a Mouse Model of Infection. *FEMS Microbiol. Lett.* **2003**, *221*, 7–16.

(30) Priebe, G. P.; Meluleni, G. J.; Coleman, F. T.; Goldberg, J. B.; Pier, G. B. Protection against Fatal Pseudomonas Aeruginosa Pneumonia in Mice after Nasal Immunization with a Live, Attenuated AroA Deletion Mutant. *Infect. Immun.* **2003**, *71*, 1453–1461.

(31) Steinrücken, H. C.; Amrhein, N. The Herbicide Glyphosate Is a Potent Inhibitor of 5-Enolpyruvylshikimic Acid-3-Phosphate Synthase. *Biochem. Biophys. Res. Commun.* **1980**, *94*, 1207–1212.

(32) Amrhein, N.; Deus, B.; Gehrke, P.; Steinrücken, H. C. The Site of the Inhibition of the Shikimate Pathway by Glyphosate. *Plant Physiol.* **1980**, *66*, 830–834.

(33) Gunawan, J.; Simard, D.; Gilbert, M.; Lovering, A. L.; Wakarchuk, W. W.; Tanner, M. E.; Strynadka, N. C. J. Structural and mechanistic analysis of sialic acid synthase NeuB from Neisseria meningitidis in complex with Mn^{2+}, phosphoenolpyruvate, and N-acetylmannosaminitol. *J. Biol. Chem.* **2005**, *280*, 3555–3563.

(34) Wang, B.; Brand-Miller, J. The Role and Potential of Sialic Acid in Human Nutrition. *Eur. J. Clin. Nutr.* **2003**, *57*, 1351–1369.

(35) Tanner, M. E. The enzymes of sialic acid biosynthesis. *Bioorg. Chem.* **2005**, *33*, 216-228.

(36) Varki, A. Sialic Acids as Ligands in Recognition Phenomena. *FASEB J.* **1997**, *11*, 248–255.

(37) Traving, C., & Schauer, R. Structure, function and metabolism of sialic acids. Cellular and *Cell. Mol. Life. Sci.* **1998**, *54*, 1330-1349.

(38) Fukuda, M. Possible roles of tumor-associated carbohydrate antigens. *Cancer Res.* **1996**, *56*, 2237-2244.

(39) Gorelik, E., Galili, U., & Raz, A. On the role of cell surface carbohydrates and their binding proteins (lectins) in tumor metastasis. *Cancer Metast. Rev.* **2001**, *20*, 245-277.

(40) Preston, A., Mandrell, R. E., Gibson, B. W., & Apicella, M. A. The lipooligosaccharides of pathogenic gram-negative bacteria. *Crit. Rev. Microbiol.* **1996**, *22*, 139-180.

(41) Annunziato, P. W.; Wright, L. F.; Vann, W. F.; Silver, R. P. Nucleotide Sequence and Genetic Analysis of the NeuD and NeuB Genes in Region 2 of the Polysialic Acid Gene Cluster of Escherichia Coli K1. *J. Bacteriol.* **1995**, *177*, 312–319.

(42) Linton, D., Karlyshev, A. V., Hitchen, P. G., Morris, H. R., Dell, A., Gregson, N. A., & Wren, B. W. Multiple N-acetyl neuraminic acid synthetase (neuB) genes in Campylobacter jejuni: identification and characterization of the gene involved in sialylation of lipo-oligosaccharide. *Mol. Microbiol.* **2000**, *35*, 1120-1134.

(43) Angata, T.; Varki, A. Chemical Diversity in the Sialic Acids and Related α-Keto Acids: An Evolutionary Perspective. *Chem. Rev.* **2002**, *102*, 439–469.

(44) Raetz, C. R. H. Biochemistry of Endotoxins. *Annu. Rev. Biochem.* **1990**, *59*, 129–170.

(45) Radaev, S., Dastidar, P., Patel, M., Woodard, R. W., & Gatti, D. L. Structure and mechanism of 3-deoxy-D-manno-octulosonate 8-phosphate synthase. *J. Biol. Chem.* **2000**, *275*, 9476-9484.

(46) Vainer, R.; Belakhov, V.; Rabkin, E.; Baasov, T.; Adir, N. Crystal Structures of Escherichia Coli KDO8P Synthase Complexes Reveal the Source of Catalytic Irreversibility. *J. Mol. Biol.* **2005**, *351*, 641–652.

(47) Goldman, R.; Kohlbrenner, W.; Lartey, P.; Pernet, A. Antibacterial Agents Specifically Inhibiting Lipopolysaccharide Synthesis. *Nature* **1987**, *329*, 162–164.

(48) Brozek, K. A., & Raetz, C. R. Biosynthesis of lipid A in Escherichia coli. Acyl carrier protein-dependent incorporation of laurate and myristate. *J. Biol. Chem.* **1990**, *265*, 15410-15417.

(49) Vaara, M. Antibiotic-supersusceptible mutants of Escherichia coli and Salmonella typhimurium. *Antimicrob. Agents. Chemother.* **1993,** *37*, 2255.

(50) Duewel, H. S.; Woodard, R. W. A Metal Bridge between Two Enzyme Families: 3-Deoxy-D-Manno-Octulosonate-8-Phosphate Synthase from Aquifex Aeolicus Requires a Divalent Metal for Activity. *J. Biol. Chem.* **2000**, *275*, 22824–22831.

(51) Krosky, D. J.; Alm, R.; Berg, M.; Carmel, G.; Tummino, P. J.; Xu, B.; Yang, W. Helicobacter Pylori 3-Deoxy-D-Manno-Octulosonate-8-Phosphate (KDO-8-P) Synthase Is a Zinc-Metalloenzyme. *Biochim. Biophys. Acta, Protein Struct. Mol. Enzymol.* **2002**, *1594*, 297–306.

(52) Gosset, G.; Bonner, C. A.; Jensen, R. A. Microbial Origin of Plant-Type 2-Keto-3-Deoxy-D-Arabino-Heptulosonate 7-Phosphate Synthases, Exemplified by the Chorismate-and Tryptophan-Regulated Enzyme from Xanthomonas Campestris. *J. Bacteriol.* **2001**, *183*, 4061–4070.

(53) Jensen, R. A., Xie, G., Calhoun, D. H., & Bonner, C. A. The correct phylogenetic relationship of KdsA (3-deoxy-D-manno-octulosonate 8-phosphate synthase) with one of two independently evolved classes of AroA (3-deoxy-D-arabino-heptulosonate 7-phosphate synthase). *J. Mol. Evol.* **2002,** *54*, 416.

(54) Zhao, H., Gao, H., Ji, K., Yan, B., Li, Q., Mo, S., Zheng, M., Ou, Q., Wu, B., Li, N. and Jiang, C., Isolation and biochemical characterization of a metagenome-derived 3-deoxy-D-arabino-heptulosonate-7-phosphate synthase gene from subtropical marine mangrove wetland sediments. *AMB Express* **2019**, *9*, 19.

(55) Braus, G. H. Aromatic amino acid biosynthesis in the yeast Saccharomyces cerevisiae: a model system for the regulation of a eukaryotic biosynthetic pathway. *Microbiol. Mol. Biol. Rev.* **1991**, *55*, 349-370.

(56) Schnappauf, G.; Hartmann, M.; Künzler, M.; Braus, G. H. The Two 3-Deoxy-D-Arabino-Heptulosonate-7-Phosphate Synthase Isoenzymes from Saccharomyces Cerevisiae Show Different Kinetic Modes of Inhibition. *Arch. Microbiol.* **1998**, *169*, 517–524.

(57) Subramaniam, P. S.; Xie, G.; Xia, T.; Jensen, R. A. Substrate Ambiguity of 3-Deoxy-D-Manno-Octulosonate 8-Phosphate Synthase from Neisseria Gonorrhoeae in the Context of Its Membership in a Protein Family Containing a Subset of 3-Deoxy-D-Arabino-Heptulosonate 7-Phosphate Synthases. *J. Bacteriol.* **1998**, *180*, 119–127.

(58) Xu, X.; Wang, J.; Grison, C.; Petek, S.; Coutrot, P.; Birck, M.; Woodard, R.; Gatti, D. Structure-Based Design of Novel Inhibitors of 3-Deoxy-d-Manno-Octulosonate 8-Phosphate Synthase. *Drug Des. Discov.* **2003**, *18*, 91–99.

(59) Pratap, S., Dev, A., Kumar, V., Yadav, R., Narwal, M., Tomar, S., & Kumar, P. Structure of chorismate mutase-like domain of DAHPS from Bacillus subtilis complexed with novel inhibitor reveals conformational plasticity of active site. *Sci. Rep.* **2017**, *7*, 1-15.

(60) Doy, C. H.; Brown, K. D. Control of Aromatic Biosynthesis: The Multiplicity of 7-Phospho-2-Oxo-3-Deoxy-d-Arabino-Heptonated-Erythrose-4-Phosphate-Lyase(Pyruvate-Phosphorylating) in Eschetichia Coli W. *Biochim. Biophys. Acta, Gen. Subj.* **1965**, *104*, 377–389.

(61) Blackmore, N. J.; Reichau, S.; Jiao, W.; Hutton, R. D.; Baker, E. N.; Jameson, G. B.; Parker, E. J. Three Sites and You Are out: Ternary Synergistic Allostery Controls Aromatic Amino Acid Biosynthesis in Mycobacterium Tuberculosis. *J. Mol. Biol.* **2013**, *425*, 1582–1592.

(62) Herrmann, K. M.; Weaver, L. M. The shikimate pathway. *Annu. Rev. Plant Physiol. Plant Mol. Biol.* **1999**, 473–503

(63) Light, S. H.; Halavaty, A. S.; Minasov, G.; Shuvalova, L.; Anderson, W. F. Structural Analysis of a 3-Deoxy-D-Arabino-Heptulosonate 7-Phosphate Synthase with an N-Terminal Chorismate Mutase-like Regulatory Domain. *Protein Sci.* **2012**, *21*, 887–895.

(64) McCandliss, R. J.; Herrmann, K. M. Iron, an Essential Element for Biosynthesis of Aromatic Compounds. *Proc. Natl. Acad. Sci. U. S. A.* **1978**, *75*, 4810–4813.

(65) Stephens, C. M., & Bauerle, R. Analysis of the metal requirement of 3-deoxy-D-arabino-heptulosonate-7-phosphate synthase from Escherichia coli. *J. Biol. Chem.* **1991**, *266*, 20810-20817.

(66) Staub, M.; Dénes, G. Purification and Properties of the 3-Deoxy-d-Arabino-Heptulosonate-7-Phosphate Synthase (Phenylalanine Sensitive) of Escherichia Coli K12. I. Purification of

Enzyme and Some of Its Catalytic Properties. *Biochim. Biophys. Acta, Enzymol.* **1969**, *178*, 588–598.

(67) König, V.; Pfeil, A.; Braus, G. H.; Schneider, T. R. Substrate and Metal Complexes of 3-Deoxy-D-Arabino-Heptulosonate-7-Phosphate Synthase from Saccharomyces Cerevisiae Provide New Insights into the Catalytic Mechanism. *J. Mol. Biol.* **2004**, *337*, 675–690.

(68) Shumilin, I. A.; Bauerle, R.; Wu, J.; Woodard, R. W.; Kretsinger, R. H. Crystal Structure of the Reaction Complex of 3-Deoxy-D-Arabino- Heptulosonate-7-Phosphate Synthase from Thermotoga Maritima Refines the Catalytic Mechanism and Indicates a New Mechanism of Allosteric Regulation. *J. Mol. Biol.* **2004**, *341*, 455–466.

(69) Schofield, L. R.; Anderson, B. F.; Patchett, M. L.; Norris, G. E.; Jameson, G. B.; Parker, E. J. Substrate Ambiguity and Crystal Structure of Pyrococcus Furiosus 3-Deoxy-D-Arabino-Heptulosonate-7-Phosphate Synthase: An Ancestral 3-Deoxyald-2-Ulosonate-Phosphate Synthase? *Biochemistry* **2005**, *44*, 11950–11962.

(70) Shumilin, I. A.; Kretsinger, R. H.; Bauerle, R. H. Crystal Structure of Phenylalanine-Regulated 3-Deoxy-D-Arabino- Heptulosonate-7-Phosphate Synthase from Escherichia coli. *Structure* **1999**, *7*, 865–875.

(71) Stephens, C. M., & Bauerle, R. Analysis of the metal requirement of 3-deoxy-D-arabino-heptulosonate-7-phosphate synthase from Escherichia coli. *J. Biol. Chem.* **1991**, *266*, 20810-20817.

(72) Clark, M. E.; Berti, P. J. Enolpyruvyl Activation by Enolpyruvylshikimate-3-Phosphate Synthase. *Biochemistry* **2007**, *46*, 1933–1940.

(73) Balachandran, N.; Heimhalt, M.; Liuni, P.; To, F.; Wilson, D. J.; Junop, M. S.; Berti, P. J. Potent Inhibition of 3-Deoxy-d-Arabinoheptulosonate-7-Phosphate (DAHP) Synthase by DAHP Oxime, a Phosphate Group Mimic. *Biochemistry* **2016**, *55*, 6617–6629.

(74) Balachandran, N.; To, F.; Berti, P. J. Linear Free Energy Relationship Analysis of Transition State Mimicry by 3-Deoxy-D-Arabino-Heptulosonate-7-Phosphate (DAHP) Oxime, a DAHP Synthase Inhibitor and Phosphate Mimic. *Biochemistry* **2017**, *56*, 592–601.

(75) Meanwell, N. A. Synopsis of Some Recent Tactical Application of Bioisosteres in Drug Design. *J. Med. Chem.* **2011**, *54,* 2529–2591.

(76) Walker, S. R.; Parker, E. J. Synthesis and Evaluation of a Mechanism-Based Inhibitor of a 3-Deoxy-D-Arabino Heptulosonate 7-Phosphate Synthase. *Bioorg. Med. Chem. Lett.* **2006**, *16*, 2951–2954.

(77) Grison, C.; Petek, S.; Finance, C.; Coutrot, P. Synthesis and Antibacterial Activity of Mechanism-Based Inhibitors of KDO8P Synthase and DAH7P Synthase. *Carbohydr. Res.* **2005**, *340*, 529–537.

(78) Walker, S. R.; Cumming, H.; Parker, E. J. Substrate and Reaction Intermediate Mimics as Inhibitors of 3-Deoxy-d-Arabino-Heptulosonate 7-Phosphate Synthase. *Org. Biomol. Chem.* **2009**, *7*, 3031–3035.

(79) Pauling, L. Nature of Forces between Large Molecules of Biological Interest. *Nature* **1948**, *161*, 707–709.

(80) Chong, A. K. J.; Pegg, M. S.; Taylor, N. R.; von Itzstein, M. Evidence for a Sialosyl Cation Transition-state Complex in the Reaction of Sialidase from Influenza Virus. *Eur. J. Biochem.* **1992**, *207*, 335–343.

(81) Robertson, J. G. Mechanistic Basis of Enzyme-Targeted Drugs. *Biochemistry* **2005**, *44*, 5561–5571.

(82) Kicska, G. A.; Long, L.; Hörig, H.; Fairchild, C.; Tyler, P. C.; Furneaux, R. H.; Schramm, V. L.; Kaufman, H. L. Immucillin H, a Powerful Transition-State Analog Inhibitor of Purine Nucleoside Phosphorylase, Selectively Inhibits Human T Lymphocytes. *Proc. Natl. Acad. Sci. U. S. A.* **2001**, *98*, 4593–4598.

(83) Miles, R. W.; Tyler, P. C.; Furneaux, R. H.; Bagdassarian, C. K.; Schramm, V. L. One-Third-the-Sites Transition-State Inhibitors for Purine Nucleoside Phosphorylase. *Biochemistry* **1998**, *37*, 8615–8621.

(84) Schramm, V. L. Enzymatic Transition States and Transition State Analogues. *Curr. Opin. Chem. Biol.* **2005**, *15*, 604-613.

(85) Schramm, V. L. Transition States, Analogues, and Drug Development. *ACS Chem. Biol.* **2013**, *8*, 71–81.

(86) Schramm, V. L. Enzymatic Transition State Theory and Transition State Analogue Design. *J. Biol. Chem.* **2007**, *282*, 28297–28300.

(87) Schramm, V. L. Enzymatic Transition States, Transition-State Analogs, Dynamics, Thermodynamics, and Lifetimes. *Annu. Rev. Biochem.* **2011**, *80*, 703–732.

(88) Berti, P. J.; McCann, J. A. B. Toward a Detailed Understanding of Base Excision Repair Enzymes: Transition State and Mechanistic Analyses of N-Glycoside Hydrolysis and N-Glycoside Transfer. *Chem. Rev*. **2006,** *106*, 506–555.

(89) Schramm, V. L. Transition State Variation in Enzymatic Reactions. *Curr. Opin. Chem. Biol.* **2001**, *5*, 556–563.

(90) Bigeleisen, J.; Mayer, M. G. Calculation of Equilibrium Constants for Isotopic Exchange Reactions. *J. Chem. Phys.* **1947**, *15*, 261–267.

(91) Winkler, F. J. Reaction Rates of Isotopic Molecules. *Angew. Chemie* **1981**, *93*, 220–220.

(92) Chan, J.; Lewis, A. R.; Gilbert, M.; Karwaski, M.-F.; Bennet, A. J. A Direct NMR Method for the Measurement of Competitive Kinetic Isotope Effects. *Nat. Chem. Biol.* **2010**, *6*, 405–407.

(93) Berti, P. J.; Tanaka, K. S. E. Transition State Analysis Using Multiple Kinetic Isotope Effects: Mechanisms of Enzymatic and Non-Enzymatic Glycoside Hydrolysis and Transfer. *ChemInform* **2003**, *34*.

(94) Kohen, A.; Limbach, H.-H. *Isotope Effects in Chemistry and Biology*; Taylor & Francis, **2006**.

(95) Maitra, U., & Chandrasekhar, J. (1997). Use of isotopes for studying reaction mechanisms. *Resonance* **1997**, *2*, 29-37.

(96) Gu, H.; Zhang, S. Advances in Kinetic Isotope Effect Measurement Techniques for Enzyme Mechanism Study. *Molecules* **2013**, *18*, 9278–9292.

(97) Pascal, R. A.; Baum, M. W.; Wagner, C. K.; Rodgers, L. R.; Huang, D. S. Measurement of Deuterium Kinetic Isotope Effects in Organic and Biochemical Reactions by Natural Abundance Deuterium NMR Spectroscopy. *J. Am. Chem. Soc.* **1986**, *108*, 6477–6482.

(98) Singleton, D. A.; Thomas, A. A. High-Precision Simultaneous Determination of Multiple Small Kinetic Isotope Effects at Natural Abundance. *J. Am. Chem. Soc.* **1995**, *117* , 9357–9358.

(99) Lee, J. K.; Bain, A. D.; Berti, P. J. Probing the Transition States of Four Glucoside Hydrolyses with 13C Kinetic Isotope Effects Measured at Natural Abundance by NMR Spectroscopy. *J. Am. Chem. Soc.* **2004**, *126*, 3769–3776.

(100) Manning, K. A.; Sathyamoorthy, B.; Eletsky, A.; Szyperski, T.; Murkin, A. S. Highly Precise Measurement of Kinetic Isotope Effects Using ^{1}H-Detected 2D [^{13}C, ^{1}H]-HSQC NMR Spectroscopy. *J. Am. Chem. Soc.* **2012**, *134*, 20589–20592.

(101) Cavanagh, J.; Fairbrother, W. J.; Palmer III, A. G.; Skelton, N. J. *Protein NMR spectroscopy: principles and practice*. Elsevier Inc., **1995**.

(102) Wong, M. W. Vibrational Frequency Prediction Using Density Functional Theory. *Chem. Phys. Lett.* **1996**, *256*, 391–399.

(103) Holzgrabe, U. Quantitative NMR, Methods and Applications. *Encycl. Spectrosc. Spectrom.* **2010**, 2331–2339.

(104) Hollis, D. P. Quantitative Analysis of Aspirin, Phenacetin, and Caffeine Mixtures by Nuclear Magnetic Resonance Spectrometry. *Anal. Chem.* **1963**, *35*, 1682–1684.

(105) Malet-Martino, M.; Holzgrabe, U. NMR Techniques in Biomedical and Pharmaceutical Analysis. *J. Pharm. Biomed. Anal.* **2011**, *55*, 1–15.

(106) Szántay, C.; Béni, Z.; Balogh, G.; Gáti, T. The Changing Role of NMR Spectroscopy in Off-Line Impurity Identification: A Conceptual View. *TrAC Trends Anal. Chem.* **2006**, *25*, 806–820.

(107) Halabalaki, M.; Vougogiannopoulou, K.; Mikros, E.; Skaltsounis, A. L. Recent Advances and New Strategies in the NMR-Based Identification of Natural Products. *Curr. Opin. Biotechnol.* **2014**, *25*, 1–7.

(108) Simmler, C.; Napolitano, J. G.; McAlpine, J. B.; Chen, S.-N.; Pauli, G. F. Universal Quantitative NMR Analysis of Complex Natural Samples. *Curr. Opin. Biotechnol.* **2014**, *25*, 51–59.

(109) Kruk, J.; Doskocz, M.; Jodłowska, E.; Zacharzewska, A.; Łakomiec, J.; Czaja, K.; Kujawski, J. NMR Techniques in Metabolomic Studies: A Quick Overview on Examples of Utilization. *Appl. Magn. Reson.* **2017**, *48*, 1–21.

(110) Star-Lack, J., Vigneron, D. B., Pauly, J., Kurhanewicz, J., & Nelson, S. J. Improved solvent suppression and increased spatial excitation bandwidths for three-dimensional PRESS CSI using phase-compensating spectral/spatial spin-echo pulses. *J. Magn. Reson. Imaging* **1997**, *7*, 745-757.

(111) Malz, F.; Jancke, H. Validation of Quantitative NMR. *J. Pharm. Biomed. Anal.* **2005**, *38*, 813–823.

(112) Quinn, T. J. Primary Methods of Measurement and Primary Standards. *Metrologia* **1997**, *34*, 61–65.

(113) Ribeiro, A. A. 1H and 13C NMR Analysis of D-Amygdalin: Oligosaccharide Assignment and Sequencing. *Magn. Reson. Chem.* **1990**, *28*, 765–773.

(114) Kartashov, V. S.; Chernyshev, A. I.; Arzanastsev, A. P. Use of NMR Spectroscopy in the Analysis of Drugs (Review). *Pharm. Chem. J.* **1982**, *16*, 229–237.

(115) Claridge, T. D. *High-resolution NMR techniques in organic chemistry.* **2016**, Elsevier Inc., *27.*

(116) Wang, H.; Zhao, M.; Ackerman, J. L.; Song, Y. Saturation-Inversion-Recovery: A Method for T1 Measurement. *J. Magn. Reson.* **2017**, *274*, 137–143.

(117) Louro, R. O. Introduction to Biomolecular NMR and Metals. In *Practical Approaches to Biological Inorganic Chemistry*; Elsevier Inc., **2013**, 77–107.

(118) Reynolds, W. F. NMR Pulse Sequences. In *Encyclopedia of Spectroscopy and Spectrometry*; Elsevier Inc., **1999**, 1554–1567.

(119) Majumdar, R. D. A Nuclear Magnetic Resonance Spectroscopic Investigation of the Molecular Structure and Aggregation Behavior of Asphaltenes. Doctoral Dissertation, University of Lethbridge, Canada, **2015**.

(120) Runge, V. M., Clanton, J. A., Lukehart, C. M., Partain, C. L., & James Jr, A. E. Paramagnetic agents for contrast-enhanced NMR imaging: a review. *AJR Am. J. Roentgenol.* **1983**, *141*, 1209-1215.

(121) Pauli, G. F., Jaki, B. U., & Lankin, D. C. Quantitative 1H NMR: development and potential of a method for natural products analysis. *J. Nat. Prod.* **2005**, *68*, 133-149.

(122) Becker, E. D.; Ferretti, J. A.; Gambhir, P. N. Selection of Optimum Parameters for Pulse Fourier Transform Nuclear Magnetic Resonance. *Anal. Chem.* **1979**, *51*, 1413–1420

(123) Ross, A.; Salzmann, M.; Senn, H. Fast-HMQC using Ernst angle pulses: an efficient tool for screening of ligand binding to target proteins. *J. Biomol. NMR* **1997**, *10*, 389-396.

(124) Aue, W. P.; Bartholdi, E.; Ernst, R. R. Two-dimensional spectroscopy. Application to nuclear magnetic resonance. *J. Chem. Phys*. **1976**, *64*, 2229-2246.

(125) Jeener, J.; Meier, B. H.; Bachmann, P.; Ernst, R. R. Investigation of Exchange Processes by Two-Dimensional NMR Spectroscopy. *J. Chem. Phys.* **1979**, *71*, 4546–4553.

(126) Moeller, T. Periodicity and the Lanthanides and Actinides. *J. Chem. Educ.* **1970**, *47*, 417.

(127) Lauffer, R. B. Paramagnetic Metal Complexes as Water Proton Relaxation Agents for NMR Imaging: Theory and Design. *Chem. Rev.* **1987**, *87*, 901–927.

(128) Weinmann, H.; Brasch, R.; Press, W.; Wesbey, G. Characteristics of Gadolinium-DTPA Complex: A Potential NMR Contrast Agent. *Am. J. Roentgenol.* **1984**, *142*, 619–624.

(129) Solomon, I. Relaxation Processes in a System of Two Spins. *Phys. Rev.* **1955**, *99*, 559–565.

(130) Bloembergen, N. Spin Relaxation Processes in a Two-Proton System. *Phys. Rev.* **1956**, *104*, 1542–1547.

(131) Bloembergen, N.; Morgan, L. O. Proton Relaxation Times in Paramagnetic Solutions. Effects of Electron Spin Relaxation. *J. Chem. Phys.* **1961**, *34*, 842–850.

(132) Bloembergen, N.; Purcell, E. M.; Pound, R. V. Relaxation Effects in Nuclear Magnetic Resonance Absorption. *Phys. Rev.* **1948**, *73*, 679–712.

(133) Larive, C. K.; Rabenstein, D. L. Two-Dimensional1H NMR Spectroscopy of Aqueous Solutions with Elimination of the Water Resonance by Transverse Relaxation: Application to Assignment of The1H NMR Spectrum of Reduced Arginine Vasopressin. *Magn. Reson. Chem.* **1991**, *29*, 409–417.

(134) Jacobsen, N. E. *NMR spectroscopy explained: simplified theory, applications and examples for organic chemistry and structural biology*. John Wiley & Sons., **2007**.

(135) Monaretto, T.; Souza, A.; Moraes, T. B.; Bertucci-Neto, V.; Rondeau-Mouro, C.; Colnago, L. A. Enhancing Signal-to-Noise Ratio and Resolution in Low-Field NMR Relaxation Measurements Using Post-Acquisition Digital Filters. *Magn. Reson. Chem.* **2019**, *57*, 616–625.

(136) Lacy, P.; McKay, R. T.; Finkel, M.; Karnovsky, A.; Woehler, S.; Lewis, M. J.; Chang, D.; Stringer, K. A. Signal Intensities Derived from Different NMR Probes and Parameters Contribute to Variations in Quantification of Metabolites. *PLoS One* **2014**, *9*.

(137) Morris, G. A.; Barjat, H.; Home, T. J. Reference Deconvolution Methods. *Prog. Nucl. Magn. Reson. Spectrosc.* **1997**, *31*, 197–257.

(138) Schoenberger, T.; Menges, S.; Bernstein, M. A.; Pérez, M.; Seoane, F.; Sýkora, S.; Cobas, C. Improving the Performance of High-Precision QNMR Measurements by a Double Integration Procedure in Practical Cases. *Anal. Chem.* **2016**, *88*, 3836–3843.

(139) Lanzetta, P. A.; Alvarez, L. J.; Reinach, P. S.; Candia, O. A. An Improved Assay for Nanomole Amounts of Inorganic Phosphate. *Anal. Biochem.* **1979**, *100*, 95–97.

(140) Sieben, A. S.; Perlin, A. S.; Simpson, F. J. An Improved Preparative Method for D-Erythrose 4-Phosphate. *Can. J. Biochem.* **1966**, *44*, 663–669.

(141) Peris-Tortajada, M.; Puchades, R.; Maquieira, A. Determination of Reducing Sugars by the Neocuproine Method Using Flow Injection Analysis. *Food Chem.* **1992**, *43*, 65–69.

(142) Jain, V.; Biesinger, M. C.; Linford, M. R. The Gaussian-Lorentzian Sum, Product, and Convolution (Voigt) Functions in the Context of Peak Fitting X-Ray Photoelectron Spectroscopy (XPS) Narrow Scans. *Appl. Surf. Sci.* **2018**, *447*, 548–553.

(143) Colowick, S. P.; Kaplan, N. O. Biuret method for protein determination. In *Methods in enzymology*. Academic Press: New York, **1957**, *3*, 450-451.

(144) Dietrich, O.; Gaass, T.; Reiser, M. F. T1 Relaxation Time Constants, Influence of Oxygen, and the Oxygen Transfer Function of the Human Lung at 1.5 T—A Meta-Analysis. *Eur. J. Radiol.* **2017**, *86*, 252–260.

(145) Jansson, P. A. *Deconvolution: With Applications in Spectroscopy*; Academic Press: New York, **1984**.

(146) Duke, C. C.; MacLeod, J. K.; Williams, J. F. Nuclear Magnetic Resonance Studies of D-Erythrose 4-Phosphate in Aqueous Solution. Structures of the Major Contributing Monomeric and Dimeric Forms. *Carbohydr. Res.* **1981**, *95*, 1–26.